New Insights in the Production of Simulated Moon Agglutinates: the Use of Natural Zeolite-Bearing Rocks

New insight in the production of simulated Moon agglutinates: the use of natural zeolites bearing rocks

Journal:	*ACS Earth and Space Chemistry*
Manuscript ID	sp-2021-00118t.R1
Manuscript Type:	Article
Date Submitted by the Author:	n/a
Complete List of Authors:	Manzoli, Maela; University of Turin, Drug Science and Technology Tammaro, Olimpia; Politecnico di Torino Facoltà di Ingegneria Marocco, Antonello; Universita degli Studi di Cassino e del Lazio Meridionale, Department of Civil and Mechanical Engineering Bonelli, Barbara; Politecnico di Torino, Materials Science & Chemical Engineering Barrera, Gabriele; INRIM, Electromagnetism Department Tiberto, Paola; INRIM Allia, Paolo; Politecnico di Torino Velez, Jean-Charles; ONERA Midi-Pyrénées Toulouse Centre roggero, aurelien; Institut National des Sciences Appliquées de Lyon Ingénierie des Matériaux Polymères Dantras, Eric; Universite Toulouse III Paul Sabatier, Physique des Polymeres Arletti, Rossella; Università degli Studi di Modena e Reggio Emilia, Dipartimento di Scienze Chimiche e Geologiche Pansini, Michele; Universita degli Studi di Cassino e del Lazio Meridionale, Ingegneria Meccanica, Strutture, Ambiente e Territorio ESPOSITO, Serena; Politecnico di Torino, Department of Applied Science and Technology

New insight in the production of simulated Moon agglutinates: the use of natural zeolites bearing rocks

Maela, Manzoli[1], Olimpia Tammaro[2], Antonello Marocco[3], Barbara Bonelli[2], Gabriele Barrera[4], Paola Tiberto[4], Paolo Allia[2,4], Jean-Charles Matéo-Vélez[5], Aurélien Roggero[6,7], Eric Dantras[7], Rossella Arletti[8], Michele Pansini[3], Serena Esposito[2*]

[1]*Department of Drug Science and Technology, NIS Interdepartmental Centre and INSTM Unit of Torino - University of Torino, Via Giuria 9, Torino, 10125, Italy*

[2]*Department of Applied Science and Technology and INSTM Unit of Torino – Politecnico, Politecnico di Torino, Corso Duca degli Abruzzi 24, 10129, Torino, Italy.*

[3]*Department of Civil and Mechanical Engineering and INSTM Research Unit, Università degli Studi di Cassino e del Lazio Meridionale, Via G. Di Biasio 43, Cassino, FR 03043, Italy*

[4]*INRiM Torino, Advanced Materials for Metrology and Life Sciences, Strada delle Cacce 91, 10143 Torino, Italy*

[5]*ONERA, The French Aerospace Lab, 2 Avenue Edouard Belin, Toulouse, France*

[6]*Université de Lyon, CNRS, UMR 5223, Ingénierie des Matériaux Polymères, INSA Lyon F-69621 Villeurbanne, France*

[7]*CIRIMAT-Physique des Polymères, Université Toulouse 3 - Paul Sabatier, 118 route de Narbonne, Toulouse, France*

[8]*Department of Chemical and Geological Sciences, University of Modena e Reggio Emilia, Via Campi 103, 41125, Modena, Italy*

Keywords: nanocomposites; natural zeolites; lunar soil; agglutinates ; nanophase iron; magnetic properties; electric properties.

Corresponding Author: Serena Esposito (serena_esposito@polito.it)

Abstract

Two natural zeolite bearing rocks (one containing clinoptilolite, the other chabazite, phillipsite and analcime) were Fe-exchanged and thermally treated in a reducing atmosphere at 750 °C for 2 h. Two nanocomposites, formed by a dispersion of Fe nanoparticles in a ceramic matrix, were obtained. The prepared lunar dust simulants also contain Na^+, K^+, Ca^{2+}, and Mg^{2+} and other mineral phases originally present in the starting materials. The samples were fully characterized by different techniques such as atomic absorption spectrometry, X-ray powder diffraction followed by Rietveld analysis, transmission electron microscopy, N_2 adsorption/desorption isotherms at 77 K, measurements of grain size distribution, magnetic properties measurements, broadband dielectric spectroscopy, and DC conductivity measurements. The results of this characterization showed that the obtained metal-ceramic nanocomposites exhibit a chemical and mineralogical composition and electrical and magnetic properties similar to real moon dust and, thus, appear valid moon dust simulants.

1. INTRODUCTION

In the last decade a continuously increasing interest toward manned space missions to the Moon, both from public institutions, such as NASA and ESA, and the private sector, was triggered by the perspective to use it as a test bed either for missions to Mars or other airless planetary bodies and the possibility of field-applications of remote sensing instrumentation.[1–3]

The surface of airless planetary bodies is generally covered by a thick blanket of regolith, which is the result of space weathering processes, especially comminution, cementation and chemical modification by means of (micro)meteorites bombardment, solar wind, irradiation and sputtering of cosmic and galactic rays.[1] Such a thick blanket of regolith is composed by particles having dimension below 1 cm.[4,5] Moreover, its finest part (about 20 wt.%) exhibits dusty-like features and, in particular, consists of i) a coarse fraction of breathable lunar dust (2.5-10 μm) which can be deposited inside trachea and bronchiole ducts; ii) a fine fraction (0.1-2.5 μm) which can penetrate the respiratory zone and iii) an ultra-fine fraction (less than 0.1 μm) which can interact with mucous membranes or be trapped by macrophages and give rise to various serious toxic effects.[6–8] Thicknesses of typical dusty layers going from few up to 15 meters were recorded in various regions of the Moon.[8,9]

Furthermore, it should be taken into account that the harsh conditions to which all the lunar regolith fractions are subjected may result into their partial melting.[3,10,11] In particular, the molten

phase successively quenches to a glass that welds the mineral and lithic particles into aggregate grains, called "agglutinates".[12] Such harsh conditions can confer unique properties to the lunar agglutinates, namely such as electrostatic charge and high superficial reactivity. Moreover, such agglutinitic glass, with dimension ranging from a few nm to several μm, contains abundant iron particles,[1,13,14] occurring either as "globules" with mean size of 120 ± 20 nm[15] or metallic nanoscale particles (np-Fe^0) having dimensions between 3-33 nm with an average size of 7 nm.[16] It must be noted that in agglutinitic glass, iron occurs as Fe^0 or Fe^{2+} species, and not as Fe^{3+} species, like it occurs, instead, in terrestrial minerals.[12] Such Fe^0 and Fe^{2+} species may produce reactive oxygen species dangerous to human cells,[17] like hydrogen peroxide (H_2O_2) and hydroxyl radical (OH•).[18] Thus, the agglutinitic glass, bearing many metallic iron "globules" and nanoparticles can dissolve into body fluids and reduce hemoglobin Fe^{3+} species according to the Fenton reaction.[6,7,19] Finally, the review of the main features of the lunar rocks reports that agglutinitic glass is mainly formed by plagioclases and pyroxenes, with smaller amounts of pyroclastic volcanic glass beads, ilmenite and olivine minerals.[1] Its chemical, structural and textural features strongly affect the lunar dust properties, such as the particles adherence, which is also modified by both the reduced Moon gravity (1/6 terrestrial gravity) and by the barbed shape of the dust grains.[6]

The previous considerations accounted for the need of studying in deep the lunar dust properties. However, the poor availability of the actual Moon soil has determined the manufactory of several lunar dust simulants, which were carefully reviewed in our previous work.[20] From this review it was found that, despite the efforts of many skillful researchers, all the produced Moon dust simulants did not satisfactory mimic some of the features of the real lunar dust.[21] On the basis of these considerations it was thought that the patented process,[22,23] proposed by some of us, aiming at obtaining metal-ceramic (where ceramic means inorganic, non-metallic) magnetic nanocomposites from commercial zeolites, could be used to produce reliable Moon dust simulants. The process envisages two steps, *i.e.* a heavy metal (Fe, Ni, or Co) cation exchange of a commercial zeolite and a thermal treatment at relatively mild temperatures (500-850 °C range) under reducing atmosphere (2.0

vol.% H_2 in Ar).[24–29] The nanocomposites were already successfully used for other biochemical and environmental application and the same [30–33] efficient, inexpensive and scalable synthesis method was used to obtain two nanocomposites containing Fe^0 nanoparticles embedded in a glassy matrix starting from two commercial zeolites, namely zeolite X and A .[20]

The so-obtained nanocomposites, referred to as SMA_A and SMA_X (i.e. Simulated Moon Agglutinate from zeolite A and X, respectively), showed proper physico-chemical properties and magnetic and electric behavior to be considered as suitable materials to simulate the agglutinate fraction of regolith, lacking in most of lunar simulants.[20] However, with respect to real Moon dust, the two nanocomposites obtained in ref.[20] exhibited higher a Fe^0 content; lower Si/Al ratio and the presence of only Na^+ ions (whereas the main cations present in real Moon dust are Na^+, K^+, Ca^{2+}, and Mg^{2+}).[20] Luckily, the versatility and tuneability of the proposed preparation method left room to further improve the obtained results as[22,24–29] the Fe^0 content may be reduced by iterating a lower number of times the exchange procedures, a higher Si/Al ratio may be obtained by using a natural zeolite bearing rock as raw material and natural zeolites in their original composition contain Na^+, K^+, Ca^{2+}, and Mg^{2+} together with, possibly, traces of other cations.[34]

On the basis of the above considerations, a clinoptilolite bearing Epiclastite from Northern Sardinia (Italy) and a chabazite and phillipsite bearing Ignimbrite from Campania (Southern Italy) (labeled as LacBen and Cab70, respectively, for the sake of uniformity with previous works) were initially subjected to just one iteration of the Fe^{2+} exchange procedure and subsequently thermally treated at relatively mild temperatures (500-850 °C range) under reducing atmosphere (2.0 vol.% H_2 in Ar). [22,24,33,25–32] These natural zeolite bearing rocks, which were already fully characterized,[35–37] were selected on the basis of their high natural zeolite content, and huge potentiality, which gives rise to a very low cost.[38–40] Moreover, these natural zeolites bearing rocks were already well known as they were already tested in environment protection studies,[41–45] for ceramization purposes aiming at tiles production,[46–48] for producing lightweight aggregates to be used for concrete manufacture,[49–51] in

oenological refining processes,[52] in the immobilization of radionuclides,[53] as additive in animal diet,[54] as drug carriers,[55] and in solar energy storage applications.[56]

The so-obtained np-Fe^0 containing nanocomposites were characterized by means of physico-chemical, magnetic and electric techniques, in order assess whether they have the proper features to be considered as simulants of lunar regolith agglutinates.

2. MATERIALS AND METHODS

2.1 Chemicals and Materials Synthesis

The sample of Campanian Ignimbrite used in this work is a product traded by Italiana Zeoliti s. r. l. (Pigneto – Modena) under the trade-name Cab70, whereas the sample of Epiclastite (LacBen) comes from a deposit sited in Bortivuile (Sassari, Northern Sardinia). The Campanian Ignimbrite is the product of a huge eruption of the Campi Flegrei volcanic area (37,000 years b.p.). This trachytic pyroclastite is mainly constituted by scoriae and pumice set in a cineritic matrix. Two different lithofacies characterize this formation: a zeolite-bearing yellow one and a grey one, with epigenetic feldspars. The sum of chabazite (framework type CHA),[57] phillipsite (framework type PHI)[57] and analcime (framework type ANA)[57] content, generally close to 50 wt. %, in some deposits can even reach about 80 wt. %.[35–37] Overall the mineralogical analyses performed underlined that Campanian Ignimbrite is strongly heterogeneous.[39,40]

The Sardinian samples (LacBen) belong to a volcano-sedimentary succession generally resting on the Palaeozoic basement and linked to a calcalkaline eruptive activity, oligo-aquitanian in age. The circulation of hydrothermal fluids through a faults system caused the transformation of the rhyolitic glassy fraction of epiclastic and unwelded pyroclastic deposits in clinoptilolite (framework type CLI)[57], smectite and opal-CT.[35–37]

Bulk chemical analysis of the parent zeolites (reported in Table 1) were performed by X-Ray Fluorescence (XRFS, Philips PW1400. Analytical procedures were carried out according to refs,[58–61]

Table 1: Composition of Cab70 and LacBen as obtained by XRFS

Sample	LacBen	Cab70
	Chemical composition (wt %)	
SiO_2	65.63	53.71
TiO_2	0.20	0.04
Al_2O_3	13.50	16.10
Fe_2O_3	1.06	4.01
MnO	0.01	0.02
MgO	1.04	1.01
CaO	2.49	4.01
Na_2O	2.46	2.06
K_2O	1.11	7.03
P_2O_5	tr.	0.01
H_2O	12.50	12.00

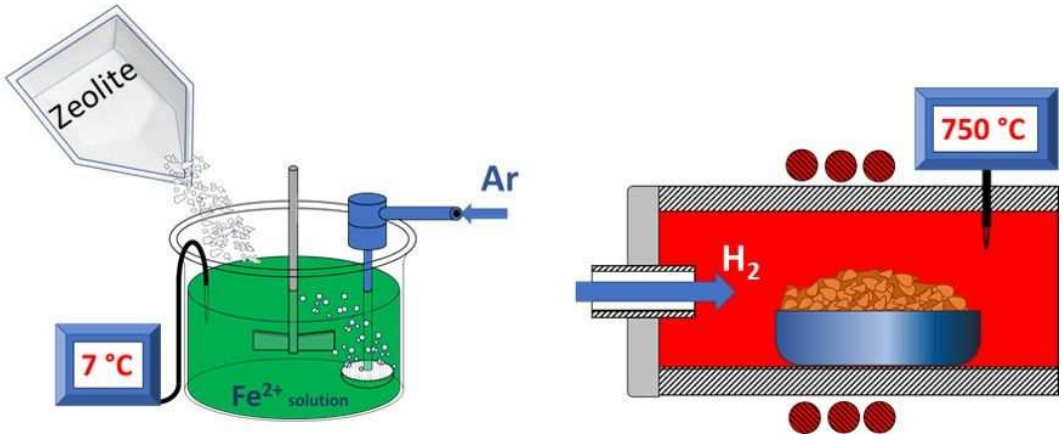

Scheme 1. Sketch of the preparation procedure of both SMA_Cab70 and SMA_LacBen by Fe^{2+} cation exchange of Cab70 and LacBen zeolite followed by reductive thermal treatment at 750 °C.

The natural zeolite bearing materials Cab70 and LacBen were subjected to the adopted preparation procedure shown in Scheme 1: the natural zeolite bearing material was contacted with a 0.1 M Fe^{2+} solution (pH = 3.8), prepared by dissolving $FeSO_4 \cdot 7H_2O$ (Aldrich, 99.5 wt. %) in doubly distilled water (solid/liquid weight ratio = 1/50 g/g; contact time t = 2 h). To prevent Fe^{2+} oxidation, during the ionic exchange the temperature was kept at about 7 °C and Ar was continuously bubbled into the solution.[62] The solid was then recovered by filtration, washed with doubly distilled water, dried for about one day at 80 °C and eventually stored for at least 3 days in a 50% relative humidity environment (created by a saturated $Ca(NO_3)_2$ aqueous solution), to allow water saturation of the zeolite(s). Afterwards, the Fe^{2+} exchanged natural zeolite bearing materials (hereafter referred to as Fe-Cab70 and Fe-LacBen) were treated in a Pt crucible at 750 °C for 2 h (heating rate 15 degrees

min^{-1}) by flowing a 2 vol.% H_2 in Ar mixture inside an Al_2O_3 tubular furnace (inner diameter = 6.9 cm, height = 91 cm). Afterwards, the furnace was switched off and the samples were left to cool down to room temperature (r.t.).

The two nanocomposites obtained from the Cab70 and LacBen natural zeolite bearing materials will be hereafter referred to as SMA_Cab70 and SMA_LacBen, respectively (SMA stands for Simulated Moon Agglutinate).

2.2 Characterization Methods

The content of Fe^{2+} and (residual) Na^+, K^+, Ca^{2+}, and Mg^{2+} in both Fe-Cab70 and Fe-LacBen samples was determined by atomic absorption spectrophotometry (AAS, Perkin-Elmer Analyst 100 apparatus) after dissolving the solids in a 40 wt.% HF and 14 wt.% $HClO_4$ aqueous solution.[63,64]

Quantitative phase analyses (QPA) were carried out on the parent materials (LacBen, Cab70), on the Fe-exchanged materials (Fe-LacBen, Fe-Cab70) and on the nanocomposites (SMA_ LacBen, SMA_Cab70) by exploiting synchrotron radiation: the synchrotron X-ray powder diffraction (XRPD) patterns were collected on the XRD1 beamline at Elettra Sincrotrone Trieste (Italy) with a fixed wavelength of 0.70 Å. The powders were packed along with Al_2O_3 (10 wt.%) as internal standard in a boron capillary and spun under the beam. The diffraction patterns were collected using a Dectris Pilatus 2M detector. The combined RIR-Rietveld method, which enables the QPA and the calculation of both the crystalline and amorphous fractions,[65] was performed by using the GSAS package[66] with the EXPGUI interface.[67] The results of QPA on the six analysed samples is reported in table 2.

N_2 adsorption/desorption isotherms at 77 K were measured on samples previously outgassed at 200 °C for 3h to remove water and other atmospheric contaminants (Micrometrics ASAP 2020Plus). The samples specific surface area was calculated according to the Brunauer–Emmett–Teller (BET) method (S_{BET}); total pore volume (V_p) and micropore volume (V_{mp}) were determined from the amount of adsorbed N_2 at $P/P_0 = 0.9$ and according to the *t*-plot method, respectively.

Transmission electron microscopy (TEM) characterization was performed by using a side entry JEOL 3010-UHR microscope operating at 300 kV, equipped with a LaB6 filament, a (2k×2k)-pixel Gatan US1000 CCD camera and an OXFORD INCA EDS instrument for atomic recognition via energy dispersive spectroscopy (EDS). To prepare the samples, the powders were either briefly contacted with lacey carbon Cu grids, which resulted in the mere electrostatic adhesion of some particles to the sample holder. Particle size distribution and mean particle diameter (d_m) of np-Fe^0 were obtained by considering a statistically representative number of particles (200-400 nanoparticles) on several TEM images (at least 30 different images). In particular, the d_m was calculated using the following equation:

$$d_m = \Sigma d_i n_i / \Sigma n_i \quad (1)$$

where n_i is the number of particles of diameter d_i. It is worth noting that both exchanged Fe-Cab70 and Fe-LacBen samples were stable to prolonged exposition under the electron beam of the instrument (no metal coalescence, nor modification of the zeolitic framework were observed during the measurements.

Differential centrifugal sedimentation method was applied to calculate the particle size distribution on a disc centrifuge (CPS DC24000). Before the measurements, a defined aliquot of samples was dispersed in water and sonicated for 5 min. A particle density of 2.0 mg ml^{-1} and a refractive index of 1.48 have been used for all the measurement with a non-sphericity factor of 1 (assuming a spherical form). The particle absorption values have been varied because of the different color of the samples, namely 0.1 for LacBen, Fe-LacBen and CAB70, 0.4 for Fe-CAB70 and 1.0 for SMA_Cab70 and SMA_LacBen.

2.3 Magnetic and electrical properties measurement

The magnetic hysteresis loops of the SMA_Cab70 and SMA_LacBen nanocomposites were studied between 100 K and room temperature on a SQUID magnetometer operating in the 0-70 kOe

range. In order to extract further information on the Fe^0 nanoparticles, the FC/ZFC curves of both samples were measured in the temperature interval 10 - 300 K under a field of 50 Oe.

The electrical properties of the nanocomposites were studied using Broadband Dielectric Spectroscopy (BDS) and DC conductivity measurements techniques.[68,69] In both types of measurement, samples made of dust layers were approximately 200 μm thick and confined between two metallic electrodes. Isotherm dielectric spectroscopy measurements were carried out under dry N_2 flow at atmospheric pressure at the CIRIMAT laboratory (Toulouse, France) in the 133 - 423 K temperature range and in the 10^{-2} -10^6 Hz frequency range. By steps of 283 K, sinusoidal voltages U^* (amplitude 1V, 10 points per frequency decade) were isothermally applied to the sample. The measurements of both the induced current (I^*) and its phase shift relative to the applied voltage yielded the complex impedance (Z^*) values as a function of temperature and frequency. The complex dielectric permittivity ε^* (eq. 2) and electrical conductivity σ^* (eq. 3) formalisms were used to represent the BDS data.

$$\varepsilon^*(\omega) = \varepsilon'(\omega) - i\varepsilon''(\omega) = \frac{1}{i\omega C_0 Z^*(\omega)} \qquad (2.1)$$

$$C_0 = \frac{\varepsilon_0 A}{l} \qquad (2.2)$$

$$\sigma^*(\omega) = \sigma'(\omega) + i\sigma''(\omega) = i\omega\varepsilon_0\varepsilon^*(\omega) \qquad (3)$$

where ε' and ε'' are the real and imaginary parts of ε^*, ω the angular frequency, and C_0 the capacitance of the vacuum-filled capacitor formed by the two electrodes of area A separated by the sample thickness l (ε_0 is the vacuum permittivity), where σ' and σ'' are the real and imaginary parts of σ^*.

DC conductivity measurements were carried out under secondary vacuum (< 10^{-6} mbar) at the ONERA laboratory (Toulouse, France) with a constant voltage between the electrodes and with temperature from 298 to 423 K. Dust layer density was around 0.6 g cm^{-3}.

3. Results and Discussion

3.1 Physico-chemical characterization

The QPA results obtained with the parent materials, reported in Table 2, confirm the literature data of samples coming from the same sites. The Cab70 sample contains three zeolitic phases, phillipsite being the most abundant one (30.4 wt. %) followed by chabazite (6.3 wt. %) and analcime (5.3 wt. %). Along with the zeolites, the sample also contains K-Feldspar (22.9 wt.%), phyllosilicates (6.3 wt.% Muscovite/illite) and a relatively high amount of amorphous phase (28.9 wt.%). The LacBen sample is a clinoptilolite zeolite (54.2 wt. %) containing a relatively high amount of K-Feldspar (22.3 wt.%), quartz (9.7wt.%), low levels of phyllosilicates (<1wt% Muscovite/illite) and a moderate amount of amorphous phase (12.8 wt.%).

As reported in Table 2, the relative phase amounts are not affected by the Fe-exchange and only minor variations in the phase wt.% are observed, probably due to minor inhomogeneity of the parent powders (e.g. the increase of the phyllosilicates and zeolitic phase in sample LacBen). Moreover, it must be considered that the contact with the acidic Fe^{2+} exchange solution might have dissolved minor amount of some constituents of the parent materials. The appearance of a new weak peak (at 5.25° 2θ) is noteworthy, as it corresponds to an iron oxide hydrate phase ($Fe_2O_3{\cdot}H_2O$), probably precipitated from the exchange solution. The peak indicates that the phase is present in very low percentage and with the Fe-LacBen sample is even not possible to quantify it from Rietveld method.

Table 2: Results of the QPA as obtained by applying the Rietveld method to synchrotorn XRPD.

Phase	LacBen (wt %)	Fe-LacBen (wt %)	SMA_LacBen (wt %)
Clinoptilolite	54.2	60.2	13.5
K-feldspar	22.3	21.5	17.9
Quartz	9.7	7.2	7.9
Cristobalite	-	-	2.9
Muscovite/Illite	0.9	2.5	1.9

$Fe_2O_3 \cdot H_2O$	-	present	-
Fe^0	-	-	0.6
Amorphous	12.8	8.6	55.2
Total	99.9	99.9	99.9

Phase	**Cab70 (wt %)**	**Fe-Cab70 (wt %)**	**SMA_Cab70 (wt %)**
Chabazite	6.3	5.7	5.0
K-Feldspar	22.9	25.0	27.9
Phillipsite	30.4	27.9	5.0
Analcime	5.3	6.4	4.1
Muscovite/Illite	6.3	3.9	4.9
$Fe_2O_3 \cdot H_2O$	-	0.4	-
Fe^0	-	-	2.7
Amorphous	28.9	30.7	50.5
Total	100.0	100.0	100.0

As expected, the thermal treatment induces strong modification on both the nanocomposites (Figure 1), the strongest effect being related to the SMA_Cab70 sample, where the content of phillipsite drops from 30.4 to 5.0 wt. %, whereas the analcime and chabazite contents seem to be less affected by the thermal treatment, being stable up to about 800 °C. [70] The clinoptilolite content in sample LacBen strongly decreases after the thermal treatment: such a behavior, somehow slightly inconsistent with the thermal behavior of clinoptilolite (stable up to 900-1000 °C),[70] has to be ascribed to the Fe-exchange procedure that leads to a more unstable zeolite. It has been indeed demonstrated that the type of extra-framework cation occurring in the clinoptilolite porosities strongly affects its thermal behavior.[37] It must be noticed that the amount of phases other than zeolites, present in the parent materials, do not show large variations owing to the thermal treatment as they exhibit a thermal stability higher than the considered zeolites.[35–37]

Moreover, it must be borne in mind that the overall mineralogical composition of the two Moon dust simulants appears similar to the one of real Moon dust as reported by Loftus et al.[4]

Both the nanocomposites showed the presence of some Fe^0, the highest amount (2.7 wt. %) being related to the SMA_Cab70 sample. The different amount of Fe found in the two samples could

be, however, due to the dimension of the particles, being X-ray powder diffraction not very effective in quantifying nano-phases (if the diffraction domains are to small).

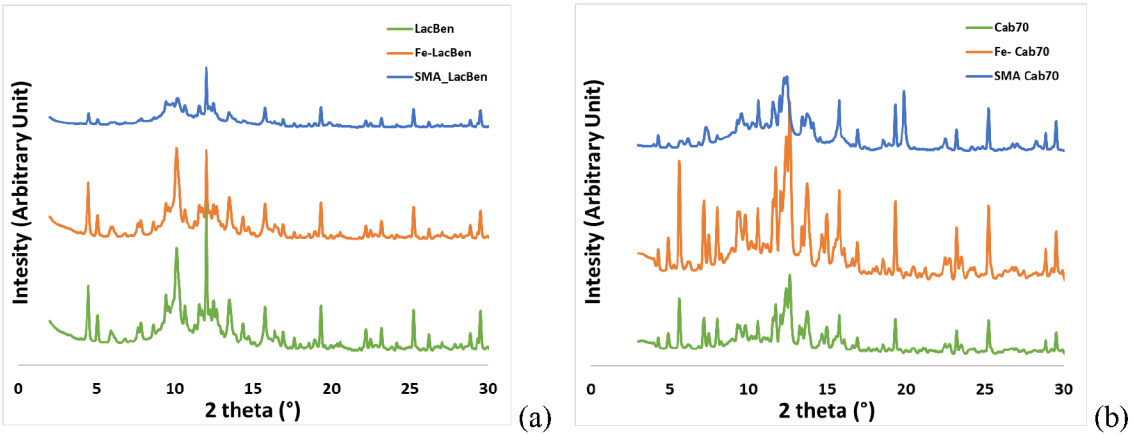

Figure 1. XRPD patterns collected of the investigated samples: (a) LacBen, Fe-LacBen and SMA_LacBen; (b) Cab70, Fe-Cab70 and SMA_Cab70

According to AAS analysis, the Fe-Cab70 and Fe-LacBen samples contain 1.79 and 0.89 meq g^{-1} Fe^{2+}, respectively, due to partial exchange of Na^+, K^+, Ca^{2+}, and Mg^{2+} present in the framework of the zeolitic phases. Apparently, the content of alkali- and alkali-metal cations after Fe^{2+} exchange turns out lower than the one present in the parent Cab70 and LacBen, but remains sizable. However, the amount of Na^+, K^+, Ca^{2+}, and Mg^{2+} present in the framework Fe-exchanged Cab70 and LacBen remains considerable as: 1) the amount of exchanged Fe^{2+} is not sufficient to exchange for all the cation exchange capacity of zeolites;[34–37] 2) in Cab70 and LacBen samples there are also other phases that do not exhibit cation exchange properties and, thus, keep their original cation composition and 3) a portion of the iron introduced in the solution for the cation exchange crystallizes as iron oxide hydrate ($Fe_2O_3 \cdot H_2O$) and thus, does not contribute to the Na^+, K^+, Ca^{2+}, and Mg^{2+} cation exchange (see above).

From these data, the overall iron wt. % in SMA_Cab70 and SMA_LacBen, was calculated considering the nanocomposites as completely dehydrated materials, resulting 5.7 and 2.9 wt. %, respectively. The different iron content in the two Fe^{2+}- exchanged zeolites is probably determined by their different cation exchange capacity, and kinetics of exchange. It must be borne in mind that

these percentages of iron encompass also the Fe present in Cab70 and LacBen samples in their original cation composition (see Table 1), i.e. before the Fe-exchange. However, such Fe is likely present in the various crystalline and amorphous phases of Cab70 and LacBen samples as trivalent iron. Clearly, such trivalent iron does not appear prone to undergo reduction as it is not a cation bound to the negative framework of a zeolite by an ionic bond weakened by the dielectric action of water molecules shielding it.

The normalized grain size distribution curves and the relative cumulative curves, in the 0.1-30 μm range, obtained by CPS are reported in Figure 2. Only one main peak is observed in all the samples but the effect of the iron exchange and subsequent heat treatment is different in the two series. Indeed, in the case of Cab70 series (Fig. 2b), the peak position is very close in all samples. The peak value of Cab70 is about 5μm with 50 wt % grain smaller than 3.3 μm (dotted green curve); small changes are made by the exchange and Fe-Cab70 shows 50 wt. % grain smaller than 3.8 μm, (dotted orange curve). The grain size distribution curve shifts to slightly higher values for the sample heat treated at 750 °C, SMA_Cab70, (50 wt. % grain smaller than 4.5 μm, dotted blue curve). Instead, for the LacBen series a shift in the peak position is clearly visible (Fig. 2a). The pristine material LacBen shows a peak at 7.3 μm with a shoulder at 1 μm and 50 wt. % grain size smaller than 5.5 μm, dotted green curve. The finest fraction of the powder is lost with the exchange operations and the maximum of the grain size distribution curve of the sample Fe-LacBen moves to 10.6 μm with 50 wt% grain smaller than 7.7 μm, dotted orange curve. The Moon dust simulant prepared starting from LacBen, SMA_LacBen, shows the main peak at 6.3 μm with 50 wt% grain smaller than 5 μm, dotted blue curve, suggesting that the heat treatment causes a finer fraction to be formed.

The grain size distribution curves of Fig. 2 allow the following considerations:

1) The parent materials Cab 70 and Lac Ben used in this work to manufacture the moon dust simulants exhibits a grain size distribution slightly finer than the one of the zeolite A used in our previous work.[20,60]

2) The grain size distribution of SMA_LacBen and SMA_Cab70 appears slightly finer than the one SMA_A and similar to the one of SMA_X of our previous work.[20]

3) SMA_LacBen and SMA_Cab70, like SMA_A and SMA_X, exhibit a grain size distribution similar to that of lunar soil coarse fraction (2.5-10 μm) but still larger than the one of fine (0.1-2.5 μm) and ultrafine (< 0.1 μm) fractions. However, for studies requiring smaller grain size, proper ball milling procedures applied to the present nanocomposites or to their parent materials could allow decreasing the grain size down to 300 nm, thus overcoming this limit.[71]

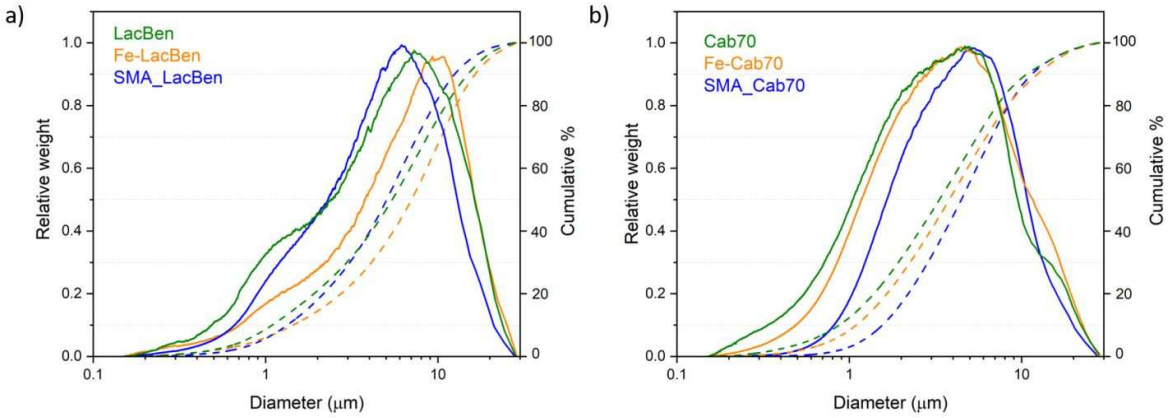

Figure 2. Normalized grain size distribution plots (solid curves) and cumulative curves (dotted curves) for Cab70 (a) and LacBen samples (b).

The N_2 adsorption/desorption isotherms of SMA_Cab70 and SMA_LacBen are reported in Fig. 3, whereas those of the parent Cab70 and LacBen samples and of the exchanged samples, Fe-Cab70 and Fe-LacBen are reported in Figure SI-1. The shape of the isotherms corresponds to type II according to the (IUPAC) classification characterized by no saturation at P/P^0 values close to 1. The classification of the isotherms is not straightforward because although the shape resembles a type II isotherm, the presence of a hysteresis would indicate a type IV isotherm. This type II isotherm commonly observed in non-porous adsorbents or adsorbents possessing relatively large pores, was in accordance with the literature data for the current zeolite phases.[72,73] The hysteresis loops are

classified as Type H3 suggesting that the porosity is caused by the aggregates of the plate-like particles, which bring about slit-shaped pores.

According to Sing's work, the isotherms can be classified as pseudo-type II, describing delayed capillary condensation due to the small rigidity of the aggregate structure of the adsorbent.[74]

The textural properties derived by the isotherms, i.e. the values of surface area (S_{BET}), total pore volume (V_p) and micropore volume (V_{mp}) are reported in Table 3. The trend of the surface area values for both sets of samples may initially appear unexpected. Indeed, the surface area increases after iron exchange, and then decreases after the thermal treatment. The second phenomenon is the result of the expected material densification in the nanocomposites, whereas the increase of area after Fe exchange is less straightforward. A possible explanation can be found in the partial dissolution of some mineral phases contained in the starting samples, Table 2, caused by the acid pH of the exchange solutions (3.8), with a consequent increase in the percentage of porous fraction.

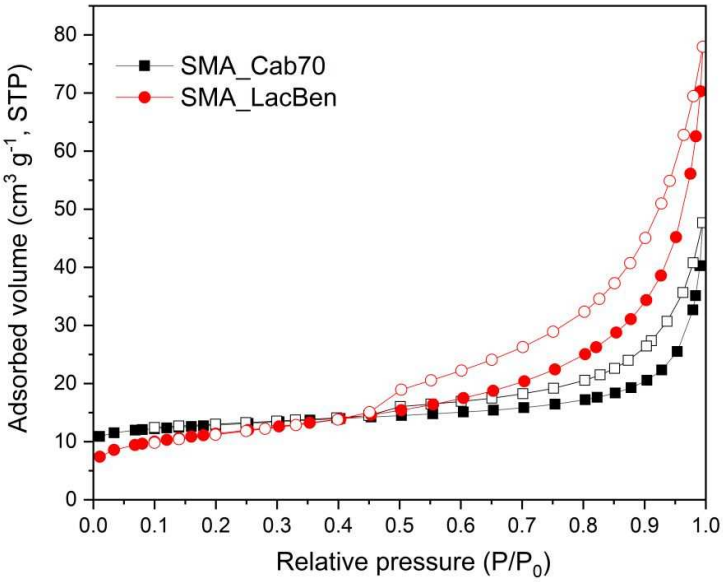

Figure 3. N_2 adsorption-desorption isotherms at 77 K of SMA_Cab70 and SMA_LacBen materials.

Table 3: BET Specific surface area (S_{BET}); total pore volume (V_p); micropore volume (V_{mp}), as obtained by N_2 isotherms at 77 K.

Sample	S_{BET} (m^2 g^{-1})	V_p (cm^3 g^{-1})	V_{mp} (cm^3 g^{-1})
Cab70	38.45	0.064	0.013
Fe_ Cab70	45.31	0.077	0.013

SMA_ Cab70	20.49	0.066	5 x10^{-3}
Lac-Ben	39.94	0.120	3 x10^{-3}
Fe _Lac-Ben	85.52	0.230	8 x10^{-3}
SMA_Lac-Ben	27.44	0.102	-

A detailed TEM and HR-TEM characterization has been carried out on the Fe-LacBen and Fe-Cab70 samples and on the nanocomposites (SMA_LacBen and SMA_Cab70, with the aim of following the morphological and structural evolution of the materials during the formation of the Fe-containing nanocomposites. In addition, particular attention was devoted to the determination of the dispersion of Fe. The results of the characterization performed on Fe-LacBen and Fe-Cab70 are shown in Figure 4 and Figure 5, respectively. The former sample appears composed by large zeolitic particles with globular shape alternate to elongated ones (Figure 4, panels a-c). In addition, highly dispersed nanoparticles, possibly iron oxide hydrate ($Fe_2O_3 \cdot H_2O$), appearing with dark contrast with respect to the zeolitic framework and with mean diameter $d_m = 2.7 \pm 1.0$ nm (Figure 4, inset of panel e) were easily recognizable as can be appreciated in panels b and d of Figure 4 and in Figure SI-2, in which an image at high magnification is reported. According to the particle size distribution, the majority of these nanoparticles has size between 2 and 3 nm. The EDS analysis confirmed the presence of iron-containing nanoparticles (Figure 4, panel e) as well as its quite uniform relative spatial distribution sample, as measured in several regions of the material (an example is shown in Figure SI-3). Moreover, the nanoparticles tend also to form agglomerates with spherical shape and with size in the 10—20 nm range, as those shown in panel c of Figure 4, therefore lowering the metal exposed surface area. Finally, EDS mapping also revealed the presence of residual cations, which did not contribute to the exchange with iron, in agreement with the results of the AAS analysis.

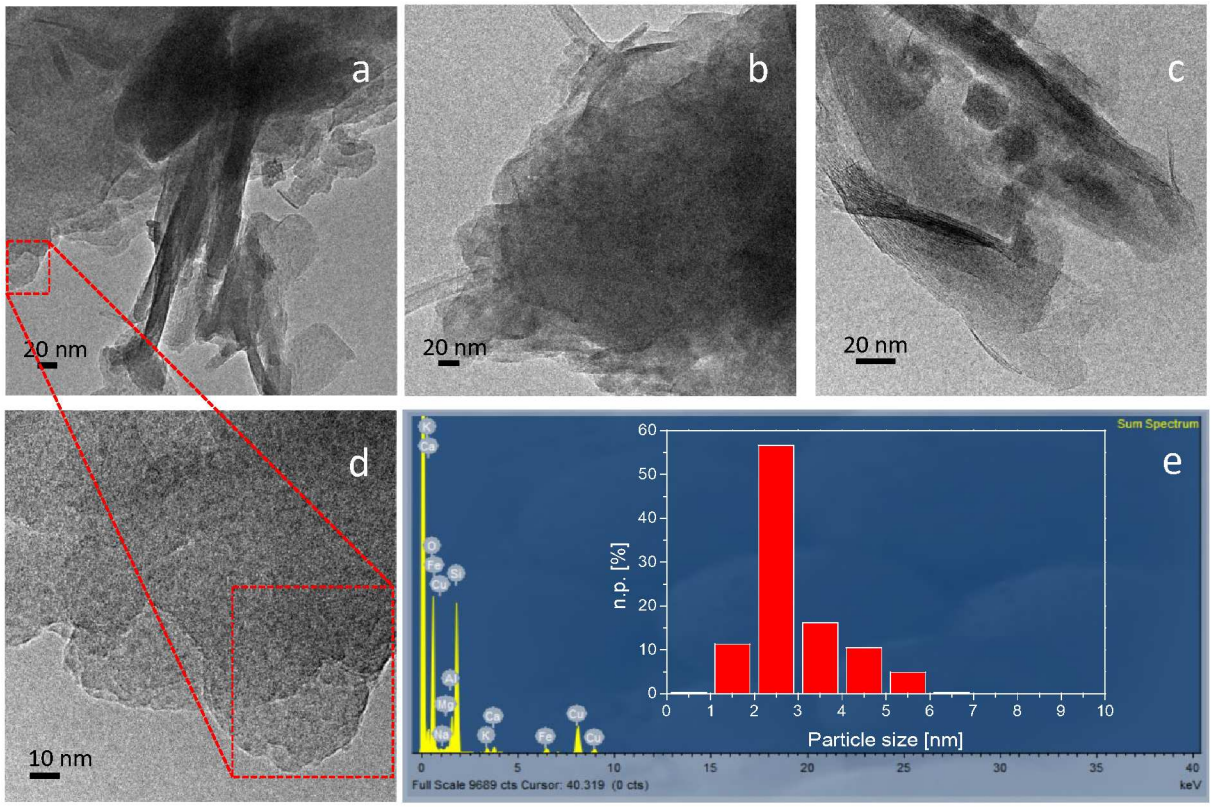

Figure 4. Representative TEM images of Fe-LacBen sample (a-c). Zoom on the region shown in a highlighted by the red box (d). EDS spectrum collected on the region shown in panel d (e) and Fe particle size distribution (inset). Instrumental magnification: 50000× (a and b), 100000× (c) and 150000× (d).

Overall, the morphology of the Fe-Cab70 material is similar to that observed for the exchanged Fe-LacBen sample, but in this case the Fe-containing nanoparticles have average diameter $d_m = 3.1 \pm 0.7$ nm (inset in panel c of Figure 5) and appeared more abundant than on the Fe-LacBen material, according to the results of the EDS analysis that indicated that the relative amount of iron present on this sample is higher than that found on the LacBen material.

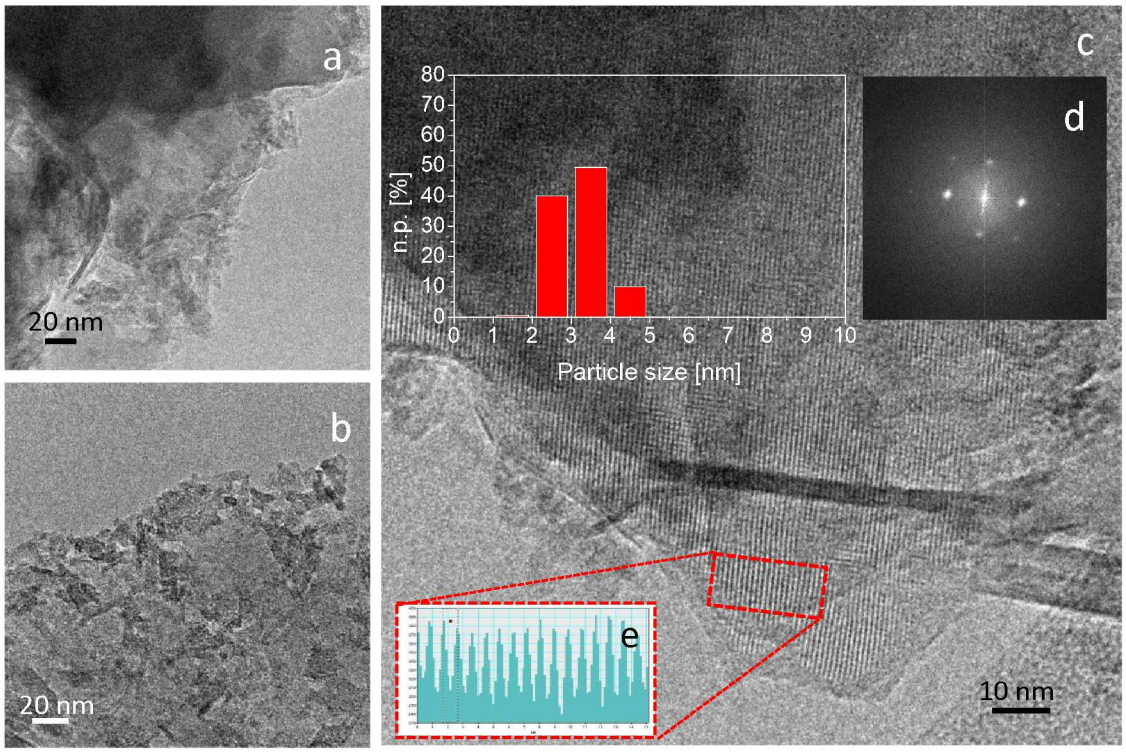

Figure 5. Representative TEM (a and b) and HR-TEM (c) images of the Fe-Cab70 sample. Inset in panel c: Fe particle size distribution. Fourier Transform of the HR-TEM image reported in panel c (d) and evaluation of the distance among the diffraction fringes (e). Instrumental magnification: 80000× (a), 100000× (b) and 150000× (c).

In addition, analogously to what previously observed, the Fe-containing nanoparticles were organized as small agglomerates (Figure 5, panels a-c and Figure SI-4). Nevertheless, such nanoparticles appear homogeneously distributed within the zeolitic matrix as demonstrated by EDS mapping reported in Figure SI-6. Many regions of the sample appear crystalline, as shown in Figure 5 (panel c) in which diffraction fringes with spacing of 9.3 Å that can be attributed to the (101) plane of rhombohedral chabazite (JCPDS file number 00-002-0062) have been measured, according to the corresponding FT and to the measure of the spacing shown in panel d and e, respectively.

Upon thermal treatment under reducing atmosphere, the Fe-containing nanoparticles previously observed on the exchanged Lacben sample undergo coalescence giving rise to a nanocomposite made up by a reduced metallic phase that appears embedded in the zeolitic framework, as shown in Figures 6 and SI-6. Particularly, an evolution to small rounded Fe nanoparticles signalled by red harrows in the Figure and with average diameter of 4.4 ± 1.7 nm (panel a), and to large Fe

particles with rounded globular shape and size ranging between about 15 and 75 nm has been observed (panels b and c).

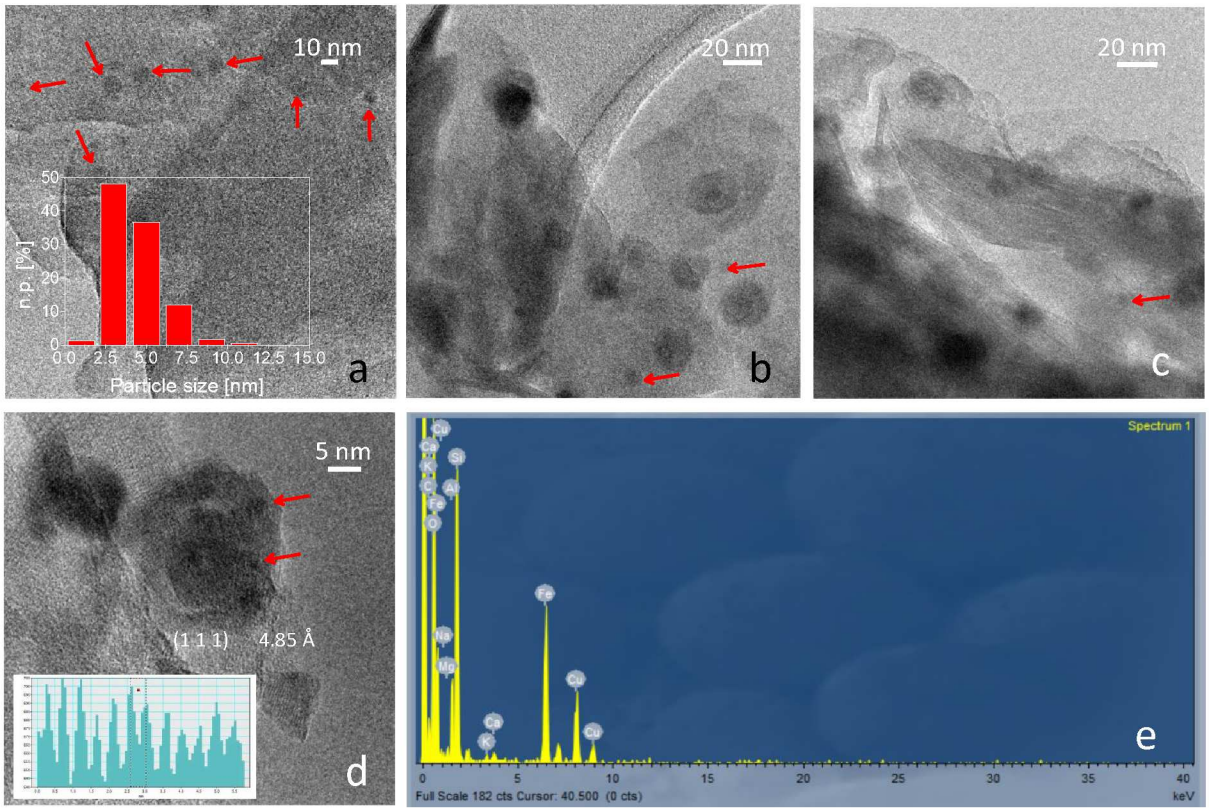

Figure 6. Representative TEM (a-c), HR-TEM (d) images, Fe particle size distribution (inset in panel a) and evaluation of the distance among the diffraction fringes (inset in d) of the SMA_Lacben sample. EDS spectrum collected on the big Fe particle shown in panel d (e). The small Fe nanoparticles are indicated by red arrows. Instrumental magnification: 150000× (a, b and c), and 300000× (d).

Moreover, these larger Fe nanoparticles display a core-shell-like morphology (panels b and c of Figure 6 and Figure SI-7), in which the core displays a darker contrast with respect to the shell and the EDS analysis revealed an intense peak related to Fe (Figure SI-8). Diffraction fringes with spacing of 4.85 Å, related to the (1 1 1) face of Fe_3O_4 in the cubic phase (JCPDS file number 00-001-1111) were observed on the shell at higher magnification. Magnetite could have been produced from the partial reduction of the iron-containing clusters with hydrogen at high temperature according to the following reaction:

$$3Fe_2O_3 + H_2 \rightarrow 2Fe_3O_4 + H_2O \qquad (4)$$

Basing on these findings, a core-shell-like morphology in which a metallic Fe^0 core is surrounded by a Fe_3O_4 shell can be hypothesized after thermal treatment.

It is worth noting that HR-TEM revealed presence of Fe_3O_4 in contrast QFA results. This can be explained by assuming that Fe_3O_4 is mainly not crystalline and/or that the amount of crystalline Fe_3O_4 is below the XRD detection limit.

Also, for the Fe-Cab70 sample, the reducing thermal led to the formation of both small and larger Fe particles within the zeolitic matrix (Figures 7, SI-8, SI-9 and SI-10). Indeed, the SMA_Cab70 material display a less dispersed metallic phase, with average size of 7.3 ± 2.0 nm, as revealed by the particle size distribution reported in panel a of Figure 7. In addition, rounded big Fe particles with core-shell morphology and size around 40-80 nm were observed also in this case. Overall, the dispersion of the metallic phase observed on the SMA_Cab70 sample is lower than that of the SMA_ LacBen sample.

It appears noteworthy that the contemporary presence of Fe^0 and Fe oxides is reported also in all real Moon dust samples.[4] Thus, it seems another point in which the obtained Moon dust simulants faithfully mimic the features of real Moon regolith.

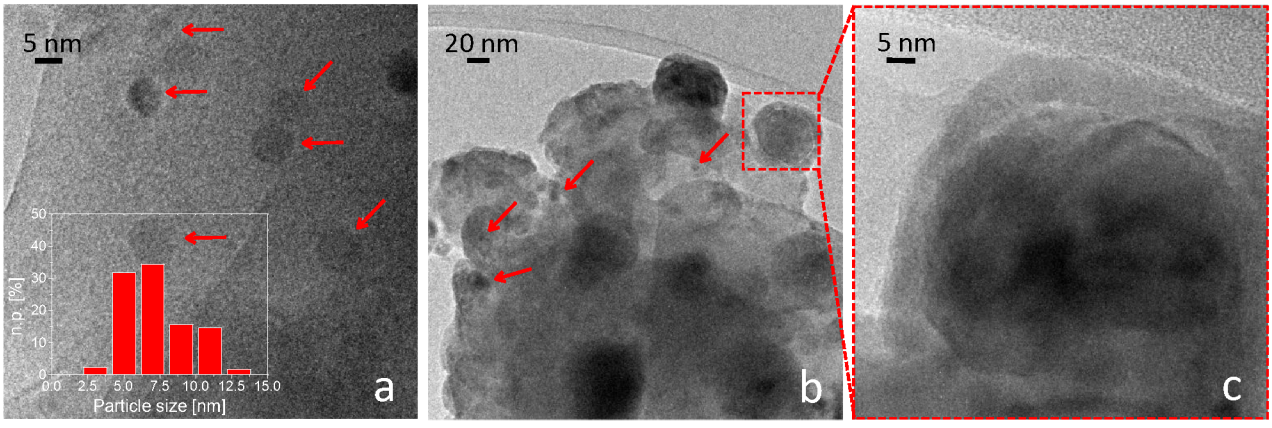

Figure 7. TEM representative images of the SMA_Cab70 sample (a, b). Zoom on the region shown in b highlighted by the red box (c). Fe particle size distribution (inset of panel a). Instrumental magnification: 250000× (a), 50000× (b) and 300000× (c).

3.2 Magnetic properties

The hysteresis loops of the two Fe-exchanged samples and of the two nanocomposites measured in the interval 100-300 K are shown in Figure 8 (panels *a,b*). The lower value corresponds to the minimum temperature typically measured at midnight on the Moon surface. In both materials, a significant magnetic signal is observed, consisting of a ferromagnetic-like contribution from iron particles followed by a paramagnetic behavior at high fields, to be ascribed to the presence of a fraction of exchanged Fe^{2+} ions still dispersed in the amorphous phase, as previously observed in similar materials[26,29] and/or to the constituents of the natural zeolite bearing materials which naturally contain Fe ions, such as the illite.[75]

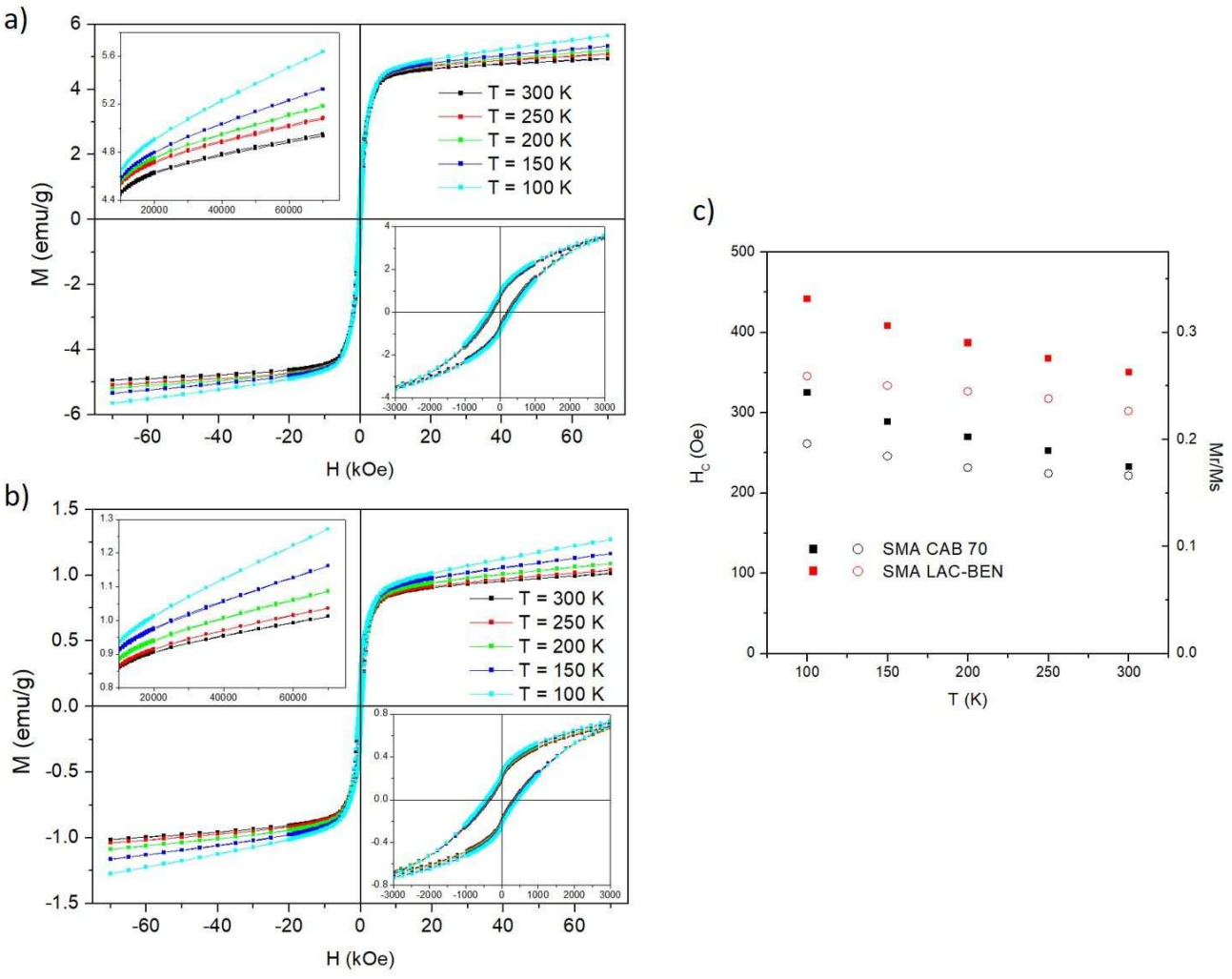

Figure 8. (a,b): hysteresis loops between T = 100 K and T = 300 K for samples SMA_Cab70 and SMA_LacBen, respectively. The insets put in evidence the paramagnetic contribution at high fields

and the shape of the loops around H = 0. (c): temperature behavior of the coercive field measured in the two samples (full symbols) and of the remanence-to saturation ratio (open symbols).

The intensity of the ferromagnetic-like signal is much larger in sample SMA_Cab70. The insets in the panels show the detail of the paramagnetic contribution (displaying the usual increase in the slope of the *M(H)* line with decreasing temperature) and the shape of the hysteresis loops close to *H = 0*, respectively. Neither the loop shape nor the loop area shows important changes in the considered temperature interval. In particular, the coercive field H_c is a weak function of temperature, as shown in panel *c*; a high value of H_c is still measured at room temperature. This suggests that a fraction of magnetic nanoparticles is still blocked at T = 300 K. The ratio M_r/M_s of remanent magnetization M_r to the saturation value of the ferromagnetic component is also reported in panel (c). Even this property turns out to be weakly dependent of temperature. Remarkably, the magnetic properties of both the nanocomposites are in good general agreement with the ones of actual lunar soils, as published elsewhere.[20]

Using the information on the content of the Fe^0 phase after thermal treatment of samples given by the QPA (rightmost column in Table I), and exploiting the asymptotic value of the room-temperature *M(H)* curves at high field (after proper subtraction of the paramagnetic contribution), we obtain an intrinsic saturation magnetization M_s of the particle phase of about 160 emu/g and about 175 emu/g for the samples SMA_LacBen and SMA_Cab70, respectively. These values of M_s are somewhat smaller than the ones found in the literature for Fe^0 nanoparticles, which are peaked around M_s = 200 emu/g, [76–78] and are consistent with the existence of a fraction of oxidized Fe (Fe_3O_4) in the outer shell of the bigger core-shell particles, as observed by TEM in both samples.

The FC/ZFC curves obtained on both materials are shown in Figure 9. While both FC curves are almost featureless, as often observed in nanoparticle systems where the individual magnetic units (i.e., single or magnetically correlated particles) are characterized by a wide distribution of blocking temperatures, [79] the ZFC curves exhibit peculiar features: in SMA_Cab70 the ZFC magnetization

increases monotonically, whereas in sample SMA_LacBen a very broad maximum centered at about 97 K is observed (see upper inset in the Figure).

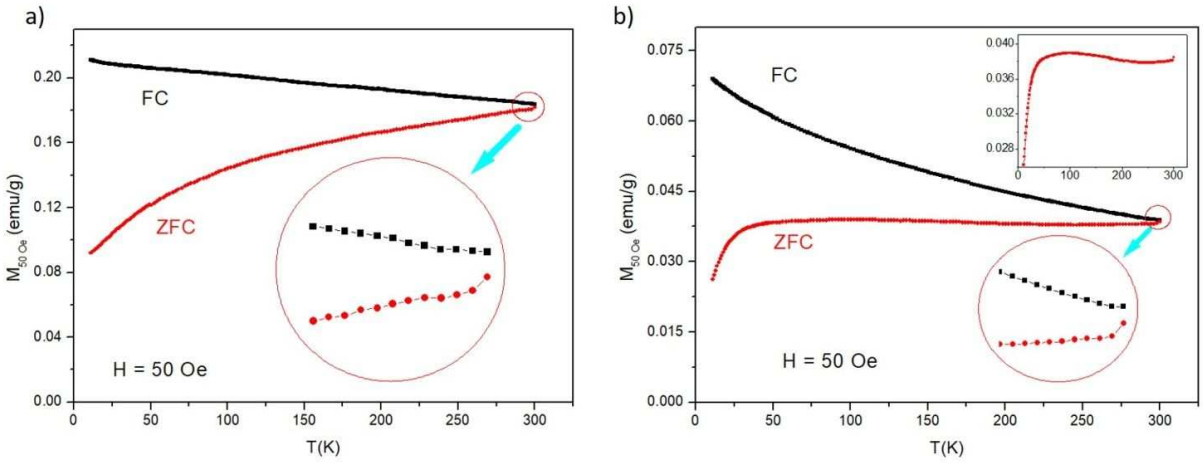

Figure 9. (a): Field-Cooled and Zero-Field–cooled magnetization curves under a field of 50 Oe for sample SMA_Cab70. The inset shows that the two curves do not touch at the starting temperature (T = 300 K); (b): the same for sample SMA_LacBen; the upper inset put in evidence the broad maximum of the ZFC curve.

As a common feature, the FC/ZFC curves are not coincident at the starting temperature of the measurement procedure (T = 300 K), as shown in the two lower insets. All these features[29,80] concur to show that a considerable fraction of individual magnetic units are still blocked at r.t., in agreement with the remarkable value of the coercive field (see above).

The difference between the shape of the ZFC curves can be ascribed to a different distribution in size of the magnetic units which individually respond to the magnetic field. Information on the particle size distribution is obtained by exploiting a standard procedure involving the derivative of the difference between ZFC and FC curves.[81,82]

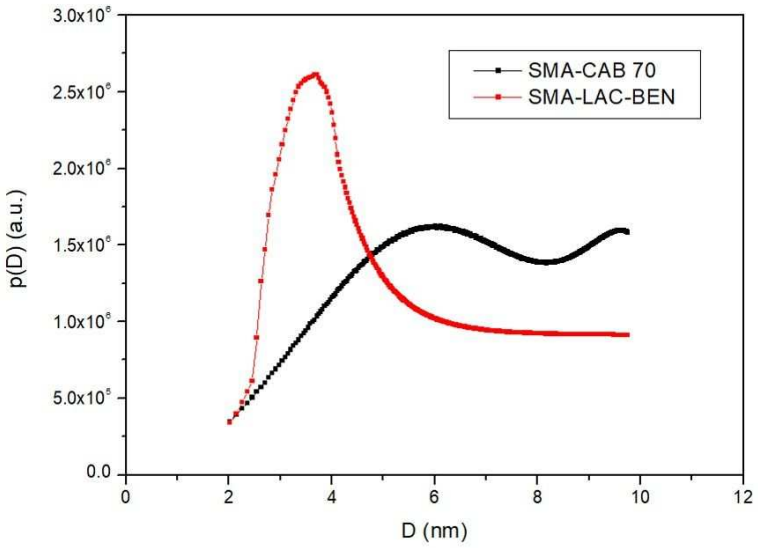

Figure 10: Size probability density p(D) (normalized to the range of existence of the two curves) for the two samples. Particles (or particle aggregates) having diameter values larger than about 10 nm are still blocked at r.t. and therefore cannot be studied by this method of analysis.

The results of this analysis are reported in Figure 10 assuming that the effective magnetic anisotropy constant of the individual Fe^0 nanoparticles takes a value $K_{eff} = 2 \times 10^6$ erg/cm^3 over the whole temperature interval, in agreement with the literature, where K_{eff} has been reported to typically range between 2×10^6 and 3.5×10^6 erg/cm^3.[83–86] In sample SMA_Cab70, the size distribution density *p(D)* monotonically increases at low *D* and reaches a kind of a plateau with weak oscillations; on the contrary, in sample SMA_LacBen the distribution exhibits a sharp peak at $D \cong 3.5$ nm followed by a plateau in the 6-10 nm interval. In both cases, the distributions show no traces of being reduced at high *D* values.

The *p(D)* curves obtained from magnetic measurements are in good general agreement with the histograms referring to the small rounded Fe^0 particles observed by HRTEM in both materials (Figures 6 and 7). Instead, the larger globular particles with core-shell structure put in evidence by the same technique are beyond the size interval covered by the analysis, the upper limit of particle sizes ($D_{max} \approx 10$ nm) being determined by the maximum temperature of FC/ZFC measurements (in this case, r.t.).

In the light of the results of HRTEM analysis reported in Section 3.1 (Figures 4-7), it is possible to draw the following picture on the basis of the magnetic properties of Fe^0 particles measured in both samples: in SMA_LacBen the sharp maximum of *p(D)* observed at small *D* values is related to the individual response of small Fe^0 particles such as the ones put in evidence in Figure 6 *(a-d*, indicated by red arrows), which can be mostly considered as weakly interacting and responding individually to the action of the magnetic field. On the other hand, the constant tail of the *p(D)* function in the interval 6-10 nm, i.e., in a size region where the histogram distribution obtained by TEM analysis is already decreasing to zero (see inset in panel *a* of Figure 6), is ascribed to the presence of a magnetic correlation among some of the small Fe^0 particles, which makes them to respond to the magnetic field as larger individual units. In fact, pairs or groups of small particles characterized by a lower than average interparticle distance *d* can behave collectively when the dipolar magnetic interaction, locally enhanced by the small value of *d*, is no longer negligible. These interacting groups are viewed by the present analysis as magnetically individual particles of slightly larger size.

On the other hand, in sample SMA_Cab70 no definite peak of the *p(D)* function emerges at low *D*. This result is in agreement with the larger histogram distribution obtained by TEM (see inset in panel *a)* of Figure 7). Moreover, the absence of a definite peak in *p(D)* can be related as well to a stronger dipolar interaction among Fe^0 particles in this sample with respect to SMA_LacBen. In fact, the larger average diameter of the individual particles determined by HRTEM (7.3 nm in this case against 4.4 nm in SMA_LacBen) and their higher concentration and lower dispersion (see Section 3.1) concur in increasing their dipolar interaction energy (which increases as the cube of *D* and as the reciprocal of the cube of *d*). The larger dipolar interaction can be instrumental in making more probable the formation of correlated pairs or clusters of particles acting as single magnetic units. This explains why a broader, less structured *p(D*) function is observed over the entire interval of diameters explored by the FC/ZFC curve analysis.

The absence of a decreasing trend of both *p(D)* curves for $D \rightarrow D_{max}$ points to the existence of a conspicuous fraction of individual magnetic units (i.e. correlated particles) whose size is larger than

10 nm. These units appear as magnetically blocked over the entire interval of investigated temperatures.

The magnetic properties of the investigated materials bear close similarities with the results of other measurements done both on actual lunar soils, simulants and synthetic materials.[14,20] All measurements point to the coexistence of various magnetic contributions in these materials, including para-, antiferro-, ferro- and superparamagnetic phases, as evidenced in the present case.[14] A comparison with a few similar materials can be found in a previous paper.[20] The saturation magnetization of the ferromagnetic phase is very close to the values reported elsewhere. [14,20] However, the coercive field values (in the 250 - 370 Oe interval around room temperature) make the present materials more similar to simulants made from a terrestrial volcanic tuff or to synthetic materials than to actual lunar soils, characterized by much lower values of Hc (less than 50 Oe).[14] This difference can be ascribed to a smaller nanoparticle size in actual lunar soils; the size analysis performed here (Figure 10) points to the existence of magnetically blocked nanoparticles having sizes much larger than 10 nm, whilst in lunar soils the low measured coercive field is coherent with the presence of almost superparamagnetic nanoparticles; however, a quantitative estimate of the size of magnetic nanoparticles is not given in the existing literature.

3.3 **Analysis of SMA_LacBen and SMA_Cab70 by broad dielectric spectroscopy**

Dielectric relaxations maps ε'' (f, T)

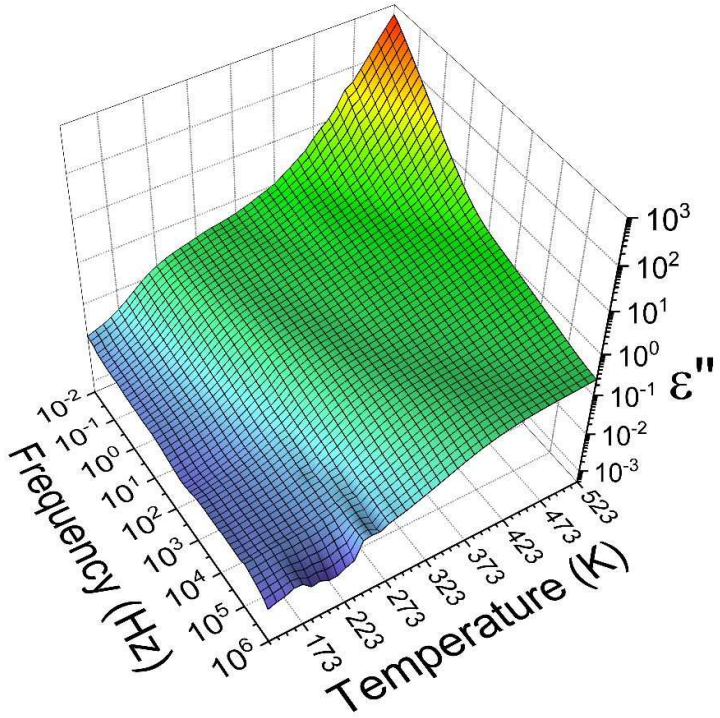

Figure 11 – Dielectric relaxation map – SMA_LacBen.

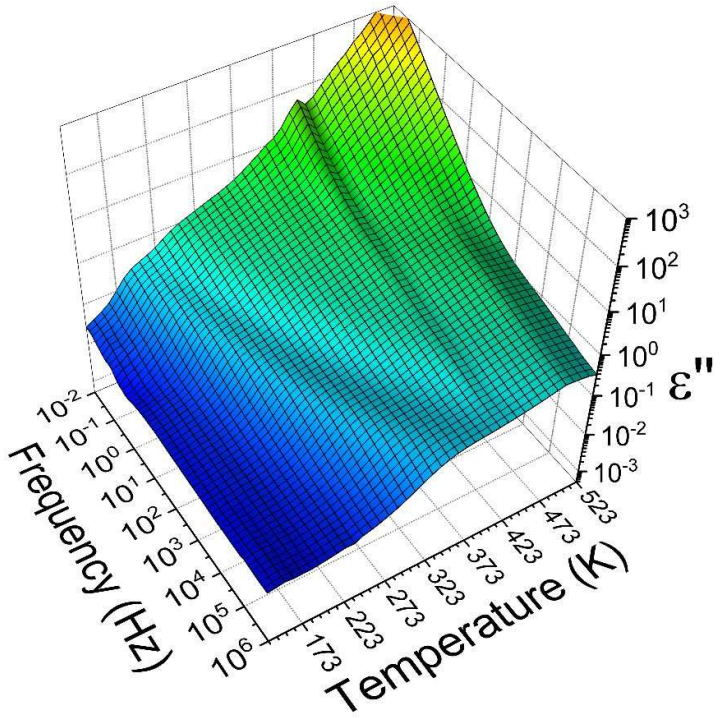

Figure 12 – Dielectric relaxation map SMA_Cab70.

The BDS map of the SMA_LacBen sample (Figure 11) shows one relaxation mode in the vicinity of 223 K at 10^{-2} Hz, that shifts towards higher frequencies as the temperature increases (in the 106 Hz range at 373 K). This mode could have various different physical origins. On one hand, it could be the manifestation of interfacial polarization phenomena, of the Maxwell-Wagner-Sillars (MWS) type, at the particle-void interfaces in the compacted powder sample. On the other hand, the mode could arise from ionic dipole-relaxations involving back and forth ion transfer between potential energy wells (by a hopping mechanism). Such relaxations have been reported for various zeolites.[87] Due to the loosely controlled packing of the particles, there is insufficient data to ascribe the dielectric mode to either of the two phenomena.

The BDS map of SMA_Cab70 (Figure 12) shows a relaxation mode similar to the one observed in SMA_LacBen, but followed by a second mode (shifted by approximately 50 K towards higher temperatures). The same discussion as for the SMA_LacBen case remains regarding the physical origins of these two modes. Because the SMA_Cab70 sample did not display enough conductivity in the range 133-423 K, additional measurements were performed in the range 413-523 K (the next day). Those measurements do not strictly overlap with the first series, probably due to water desorption during the first run, resulting in a small isothermal event visible at 413 K in Figure 12. The measurements on LacBen were performed in one run between 133 and 523 K and therefore do not display this small event.

At high temperatures and low frequencies, both moon dust simulants display a conductivity front associated with large scale transport of charge carriers across the sample.

3.4 Isothermal real conductivity spectra, σ'(f), and Arrhenius diagrams of the real conductivity values at 10-2 Hz, σ'(1000/T)

The isothermal real conductivity spectra are displayed in the temperature range 273-523 K for SMA_LacBen (Figure 13) and SMA_Cab70 (Figure 14). This representation emphasizes low-frequency charge transport processes which are expected to appear as frequency-independent

plateaus. In both cases, at sufficiently high temperature, such plateaus are observed even though they are slightly frequency dependent. The temperature dependence of the low-frequency conductivity (taken at 10^{-2} Hz) is visible in the Arrhenius diagram of Figure 15.

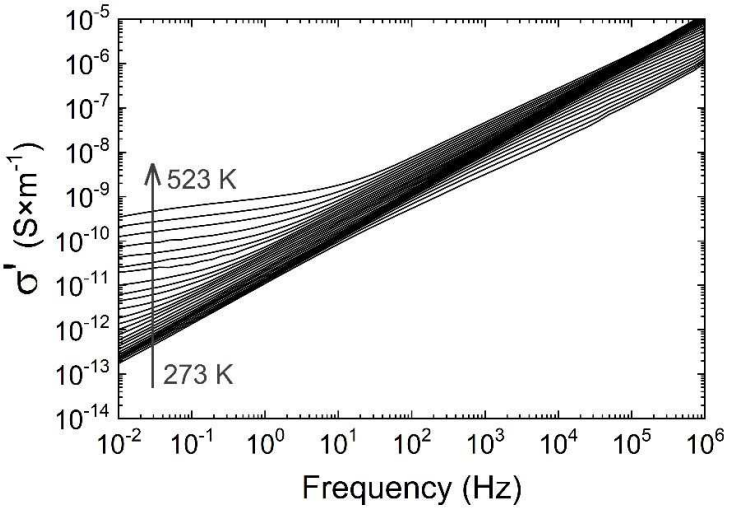

Figure 13 – Isothermal real conductivity spectra between 273 and 523 K of sample SMA_LacBen.

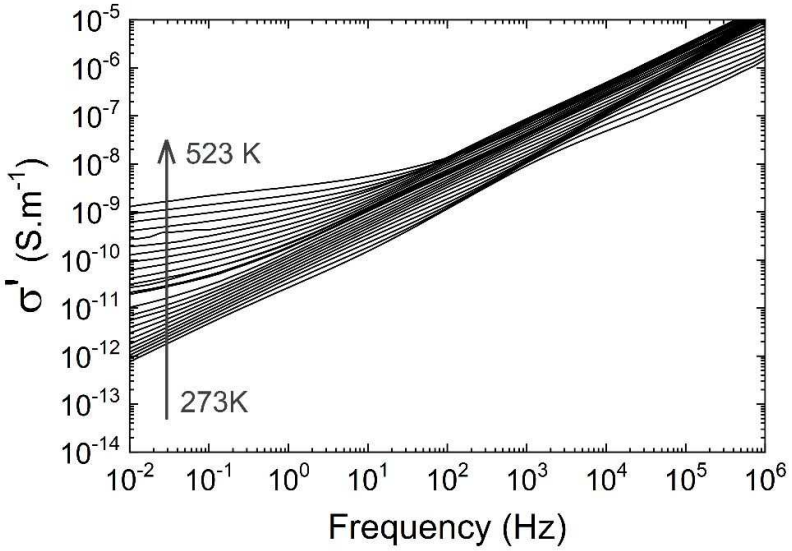

Figure 14 – Isothermal real conductivity spectra between 273 and 523 K of sample SMA_Cab70

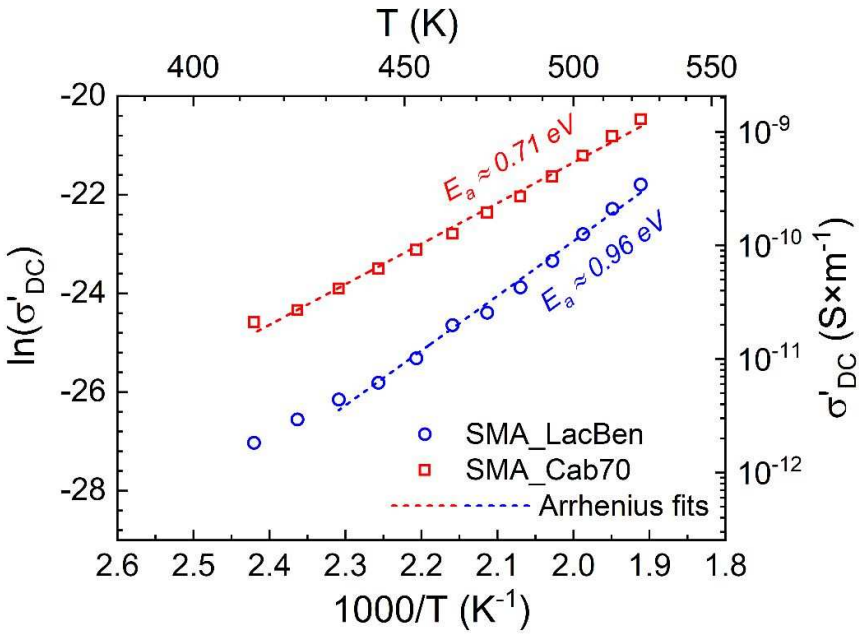

Figure 15 – Arrhenius diagram of the real conductivity at 10^{-2} Hz for SMA_LacBen and SMA_Cab70, with the corresponding Arrhenius fits and activation energies

The conductivity values of the SMA_Cab70 sample is systematically higher than that of SMA_LacBen in the temperature range 413-523 K, as can be seen in Figure 15. However, the one-decade difference between the two samples at 423 K decreases to a factor of 4 at 523 K, due to different values of the activation energy for charge transport (0.71 eV for SMA_Cab70 and 0.96 eV for SMA_LacBen).

When compared to the previously studied moon dust simulants (SMA_A and SMA_X), the SMA_LacBen and SMA_Cab70 samples are overall less conductive (sometimes by several orders of magnitude). This is why frequency independent plateaus are not observed below approximately 412 K for SMA_LacBen and SMA_Cab70 samples (as seen in Figure 13 and Figure 14) and the temperature range had to be extended up to 523 K.[20] The activation energy is 0.71 eV and 0.96 eV for SMA_Cab70 and SMA_LacBen, respectively, slightly larger than the 0.32 eV and 0.58 eV for Apollo lunar samples 15301,38 and 14613,131, respectively. The DC conductivity at 200 °C is about $3e^{-10}$ and $2e^{-11}$ S/m for SMA_Cab70 and SMA_LacBen, respectively, which is closer to the $7e^{-13}$ and $4e^{-11}$ S/m of 15301,38 and 14613,131, respectively, than DC conductivity of SMA_A and SMA_X.

CONCLUSIONS

The already good results obtained in our previous work with Moon agglutinates simulants obtained by thermally transforming, under a reducing atmosphere, Fe-exchanged zeolite A and X in metal-ceramic nanocomposites have been further improved in this work by starting from natural zeolite samples.

The following improvements were obtained in in this work:

1) A chemical composition decidedly closer to the real Moon dust was obtained.

2) A mineralogical composition decidedly closer to the real Moon dust was obtained.

3) As a consequence of obtaining an improved chemical and mineralogical composition, also the electric and magnetic behavior of the magnetic metal-ceramic nanocomposites of this work are decidedly similar to those of the real Moon dust.

Moreover, the obtained metal-ceramic nanocomposites do not appear prone to weathering as ceramic phase are well known to be stable and most of the Fe^0 nanoparticles are embedded into the ceramic matrix which protects them from oxidation.

However, this work has suggested possible further improvements of the, already good, results obtained. Actually, the Fe-exchange natural zeolite bearing material to be transformed in the metal-ceramic nanocomposite simulating the Moon dust, could be split in two portions of about equal entity. The first portion should be thermally treated under a reducing atmosphere at 750 °C, as it was done in this work, and the second portion should be thermally treated, under the same reducing atmosphere, at a decidedly higher temperature, such as 1000 °C. The thermal treatment at this temperature would result in a partial melting of the ceramic matrix which could properly mimic the effects of the meteorite bombardment on the real moon dust. Finally, the two portions of the metal-ceramic nanocomposites obtained should be mixed together to form a lone metal-ceramic nanocomposite. This resulting material should still better mimic the features of the real moon dust as also the effects of the meteorite bombardment on moon dust would be, at least partially, reproduced.

Acknowledgements

Authors thank Federico Mondino (Department of Environment, Land and Infrastructure Engineering, Politecnico di Torino, Italy) for particle size distribution analysis.

References

(1) Liu, Y.; Taylor, L. A. Characterization of Lunar Dust and a Synopsis of Available Lunar Simulants. *Planet. Space Sci.* **2011**, *59* (14), 1769–1783.

(2) WALLACE, W. T.; TAYLOR, L. A.; LIU, Y.; COOPER, B. L.; McKAY, D. S.; CHEN, B.; JEEVARAJAN, A. S. Lunar Dust and Lunar Simulant Activation and Monitoring. *Meteorit. Planet. Sci.* **2009**, *44* (7), 961–970. https://doi.org/10.1111/j.1945-5100.2009.tb00781.x.

(3) Carpenter, J. D.; Crawford, I. A.; Cockell, C.; Koschny, D.; Jaumann, R.; Wieczorek, M. Scientific Preparations for Lunar Exploration. *Planetary and Space Science*. December 2012, pp 1–2. https://doi.org/10.1016/j.pss.2012.03.001.

(4) Loftus, D. J.;Tranfield, E. M.; Rask, J. C.; McCrosssin, C. The Chemical Reactivity of Lunar Dust Relevant to Human Exploration of the Moon. *NASA Ames Research Center* https://www.lpi.usra.edu/decadal/leag/DavidJLoftus.pdf

(5) Carrier, W. D. Particle Size Distribution of Lunar Soil. *J. Geotech. Geoenvironmental Eng.* **2003**, *129* (10), 956–959. https://doi.org/10.1061/(asce)1090-0241(2003)129:10(956).

(6) Liu, Y.; Park, J.; Schnare, D. W.; Hill, E.; Taylor, L. A. . Characterization of Lunar Dust for Toxicological Studies. II: Texture and Shape Characteristic. *J. Aerosp. Eng.* **2008**, *21* (4), 272–279.

(7) Park, J.; Liu, Y.; Kihm, K. D.; Taylor, L. A. Characterization of Lunar Dust for Toxicological Studies. I: Particle Size Distribution. *J. Aerosp. Eng.* **2008**, *21* (4), 266–271.

(8) Khan-Mayberry, N. The Lunar Environment: Determining the Health Effects of Exposure to Moon Dusts. *Acta Astronaut.* **2008**, *63* (7), 1006–1014.

(9) Zhang, J.; Yang, W.; Hu, S.; Lin, Y.; Fang, G.; Li, C.; Peng, W.; Zhu, S.; He, Z.; Zhou, B.; Lin, H.; Yang, J.; Liu, E.; Xu, Y.; Wang, J.; Yao, Z.; Zou, Y.; Yan, J.; Ouyang, Z. Volcanic History of the Imbrium Basin: A Close-up View from the Lunar Rover Yutu. *Proc. Natl. Acad. Sci.* **2015**, *112* (17), 5342–5347. https://doi.org/10.1073/pnas.1503082112.

(10) Colwell, J. E.; Batiste, S.; Horányi, M.; Robertson, S.; Sture, S. Lunar Surface: Dust Dynamics and Regolith Mechanics. *Rev. Geophys* **2007**, *45* (2), 2006. https://doi.org/10.1029/2005RG000184.

(11) Caston, R.; Luc, K.; Hendrix, D.; Hurowitz, J. A.; Demple, B. Assessing Toxicity and Nuclear and Mitochondrial DNA Damage Caused by Exposure of Mammalian Cells to Lunar Regolith Simulants. *Wiley Online Libr.* **2018**, *2* (4), 139–148. https://doi.org/10.1002/2017GH000125.

(12) McKay, D. S. .; Blacic, J. D.; Center, N. J. S. Workshop on Production and Uses of Simulated Lunar Materials, LPI Technical Report 91-01. In *Workshop on Production and Uses of Simulated Lunar Materials. A Lunar and Planetary Institute Workshop*; McKay, D. S. ., Blacic, J. D., Eds.; Lunar and Planetary Institute, 3303 NASA Road 1, Houston, TX 77058: The Lunar and Planetary Institute, in Houston, Texas, 1989; Vol. 1, p 83.

(13) Wentworth, S. J.; Keller, L. P.; McKay, D. S.; Morris, R. V. Space Weathering on the Moon: Patina on Apollo 17 Samples 75075 and 76015. *Meteorit. Planet. Sci.* **1999**, *34* (4), 593–603.

(14) Liu, Y.; Taylor, L. A.; Thompson, J. R.; Schnare, D. W.; Park, J.-S. Unique Properties of Lunar Impact Glass: Nanophase Metallic Fe Synthesis. *Am. Mineral.* **2007**, *92* (8–9), 1420–

1427. https://doi.org/10.2138/am.2007.2333.

(15) James, C. L. .; Letsinger, S. L. .; Basu, A. .; Wentworth, S. J. .; McKay, D. S. Size Distribution of Fe0 Globules in Lunar Agglutinitic Glass. *33rd Annu. Lunar Planet. Sci. Conf.* **2002**.

(16) Wallace, W. T.; Phillips, C. J.; Jeevarajan, A. S.; Chen, B.; Taylor, L. A. Nanophase Iron-Enhanced Chemical Reactivity of Ground Lunar Soil. *Earth Planet. Sci. Lett.* **2010**, *295*, 571–577. https://doi.org/http://dx.doi.org/10.1016/j.epsl.2010.04.042.

(17) Fubini, B.; Hubbard, A. Reactive Oxygen Species (ROS) and Reactive Nitrogen Species (RNS) Generation by Silica in Inflammation and Fibrosis. *Free Radic. Biol. Med.* **2003**, *34* (12), 1507–1516.

(18) Hurowitz, J. A.; Tosca, N. J.; McLennan, S. M.; Schoonen, M. A. A. Production of Hydrogen Peroxide in Martian and Lunar Soils. *Earth Planet. Sci. Lett.* **2007**, *255* (1–2), 41–52.

(19) Horwell, C. J.; Fenoglio, I.; Fubini, B. Iron-Induced Hydroxyl Radical Generation from Basaltic Volcanic Ash. *Earth Planet. Sci. Lett.* **2007**, *261* (3–4), 662–669.

(20) Freyria, F. S.; Marocco, A.; Esposito, S.; Bonelli, B.; Barrera, G.; Tiberto, P.; Allia, P.; Oudayer, P.; Roggero, A.; Matéo-Vélez, J. C.; Dantras, E.; Pansini, M. Simulated Moon Agglutinates Obtained from Zeolite Precursor by Means of a Low-Cost and Scalable Synthesis Method. *ACS Earth Sp. Chem.* **2019**, *3* (9), 1884–1895. https://doi.org/10.1021/acsearthspacechem.9b00042.

(21) Witze, A. Why Planetary Scientists Want Better Fake Space Dirt. *Nature* **2017**, *547*, 146–147.

(22) Esposito, S.; Marocco, A.; Bonelli, B.; Pansini, M. Produzione Di Materiali Compositi Metallo-Ceramici Nano Strutturati Da Precursori Zeolitici. MI 2014, A000522.

(23) Esposito, S.; Marocco, A.; Bonelli, B.; Pansini, M. Production of Magnetic Metal Nanoparticles Embedded in a Silica-Alumina Matrix. World Patent WO/ 145230 A1, 2015.

(24) Marocco, A.; Dell'Agli, G.; Esposito, S.; Pansini, M. Metal-Ceramic Composite Materials from Zeolite Precursor. *Solid State Sci.* **2012**, *14* (3), 394–400. https://doi.org/10.1016/j.solidstatesciences.2012.01.006.

(25) Ronchetti, S.; Turcato, E. A.; Delmastro, A.; Esposito, S.; Ferone, C.; Pansini, M.; Onida, B.; Mazza, D. Study of the Thermal Transformations of Co- and Fe-Exchanged Zeolites A and X by "in Situ" XRD under Reducing Atmosphere. *Mater. Res. Bull.* **2010**, *45* (6), 744–750. https://doi.org/10.1016/j.materresbull.2010.02.006.

(26) Barrera, G.; Tiberto, P.; Esposito, S.; Marocco, A.; Bonelli, B.; Pansini, M.; Manzoli, M.; Allia, P. Magnetic Clustering of Ni2+ Ions in Metal-Ceramic Nanocomposites Obtained from Ni-Exchanged Zeolite Precursors. *Ceram. Int.* **2018**, *44* (14), 17240–17250. https://doi.org/10.1016/j.ceramint.2018.06.182.

(27) Esposito, S.; Dell'Agli, G.; Marocco, A.; Bonelli, B.; Allia, P.; Tiberto, P.; Barrera, G.; Manzoli, M.; Arletti, R.; Pansini, M. Magnetic Metal-Ceramic Nanocomposites Obtained from Cation-Exchanged Zeolite by Heat Treatment in Reducing Atmosphere. *Microporous Mesoporous Mater.* **2018**, *268*, 131–143. https://doi.org/10.1016/j.micromeso.2018.04.024.

(28) Barrera, G.; Tiberto, P.; Allia, P.; Bonelli, B.; Esposito, S.; Marocco, A.; Pansini, M.; Leterrier, Y. Magnetic Properties of Nanocomposites. *Appl. Sci.* **2019**, *9* (2), 212. https://doi.org/10.3390/app9020212.

(29) Barrera, G.; Allia, P.; Bonelli, B.; Esposito, S.; Freyria, F. S.; Pansini, M.; Marocco, A.; Confalonieri, G.; Arletti, R.; Tiberto, P. Magnetic Behavior of Ni Nanoparticles and Ni2+ Ions in Weakly Loaded Zeolitic Structures. *J. Alloys Compd.* **2020**, *817*, 152776. https://doi.org/10.1016/j.jallcom.2019.152776.

(30) Pansini, M.; Dell'Agli, G.; Marocco, A.; Netti, P. A.; Battista, E.; Lettera, V.; Vergara, P.; Allia, P.; Bonelli, B.; Tiberto, P.; Barrera, G.; Alberto, G.; Martra, G.; Arletti, R.; Esposito, S. Preparation and Characterization of Magnetic and Porous Metal-Ceramic Nanocomposites from a Zeolite Precursor and Their Application for DNA Separation. *J. Biomed. Nanotechnol.* **2017**, *13* (3), 337–348. https://doi.org/10.1166/jbn.2017.2345.

(31) Pansini, M.; Sannino, F.; Marocco, A.; Allia, P.; Tiberto, P.; Barrera, G.; Polisi, M.; Battista, E.; Netti, P. A.; Esposito, S. Novel Process to Prepare Magnetic Metal-Ceramic Nanocomposites from Zeolite Precursor and Their Use as Adsorbent of Agrochemicals from Water. *J. Environ. Chem. Eng.* **2018**, *6* (1), 527–538. https://doi.org/10.1016/j.jece.2017.12.030.

(32) Marocco, A.; Dell'Agli, G.; Sannino, F.; Esposito, S.; Bonelli, B.; Allia, P.; Tiberto, P.; Barrera, G.; Pansini, M. Removal of Agrochemicals from Waters by Adsorption: A Critical Comparison among Humic-Like Substances, Zeolites, Porous Oxides, and Magnetic Nanocomposites. *Processes* **2020**, *8* (2), 141. https://doi.org/10.3390/pr8020141.

(33) Esposito, S.; Marocco, A.; Dell'Agli, G.; Bonelli, B.; Mannu, F.; Allia, P.; Tiberto, P.; Barrera, G.; Pansini, M. Separation of Biological Entities from Human Blood by Using Magnetic Nanocomposites Obtained from Zeolite Precursors. *Molecules* **2020**, *25* (8), 1803. https://doi.org/10.3390/molecules25081803.

(34) Esposito, S.; Marocco, A.; Dell'Agli, G.; De Gennaro, B.; Pansini, M. Relationships between the Water Content of Zeolites and Their Cation Population. *Microporous Mesoporous Mater.* **2015**, *202*, 36–43. https://doi.org/10.1016/j.micromeso.2014.09.041.

(35) Cappelletti, P.; Langella, A.; Cruciani, G. Crystal-Chemistry and Synchrotron Rietveld Refinement of Two Different Clinoptilolites from Volcanoclastites of North-Western Sardinia. *Eur. J. Mineral.* **1999**, *11* (6), 1051–1060. https://doi.org/10.1127/ejm/11/6/1051.

(36) Cerri, G.; Langella, A.; Pansini, M.; Cappelletti, P. Methods of Determining Cation Exchange Capacities for Clinoptilolite-Rich Rocks of the Logudoro Region in Northern Sardinia, Italy. *Clays Clay Miner.* **2002**, *50* (1), 127–135. https://doi.org/10.1346/000986002761002739.

(37) Langella, A.; Pansini, M.; Cerri, G.; Cappelletti, P.; De'Gennaro, M. Thermal Behavior of Natural and Cation-Exchanged Clinoptilolite from Sardinia (Italy). *Clays Clay Miner.* **2003**, *51* (6), 625–633. https://doi.org/10.1346/CCMN.2003.0510605.

(38) Cerri, G.; Cappelletti, P.; Langella, A.; De'Gennaro, M. Zeolitization of Oligo-Miocene Volcaniclastic Rocks from Logudoro (Northern Sardinia, Italy). *Contrib. to Mineral. Petrol.* **2001**, *140* (4), 404–421. https://doi.org/10.1007/s004100000196.

(39) Cappelletti, P.; Cerri, G.; Colella, A.; de'Gennaro, M.; Langella, A.; Perrotta, A.; Scarpati, C. Post-Eruptive Processes in the Campanian Ignimbrite. *Mineral. Petrol.* **2003**, *79* (1–2), 79–

97. https://doi.org/10.1007/s00710-003-0003-7.

(40) Langella, A.; Bish, D. L.; Cappelletti, P.; Cerri, G.; Colella, A.; de Gennaro, R.; Graziano, S. F.; Perrotta, A.; Scarpati, C.; de Gennaro, M. New Insights into the Mineralogical Facies Distribution of Campanian Ignimbrite, a Relevant Italian Industrial Material. *Appl. Clay Sci.* **2013**, *72*, 55–73. https://doi.org/10.1016/j.clay.2013.01.008.

(41) Colella, C.; De' Gennaro, M.; Langella, A.; Pansini, M. Evaluation of Natural Phillipsite and Chabazite as Cation Exchangers for Copper and Zinc. *Sep. Sci. Technol.* **1998**, *33* (4), 467–481. https://doi.org/10.1080/01496399808544991.

(42) Pansini, M.; Colella, C. Dynamic Data on Lead Uptake from Water by Chabazite. *Desalination* **1990**, *78* (2), 287–295. https://doi.org/10.1016/0011-9164(90)80048-G.

(43) Albino, V.; Cioffi, R.; Pansini, M.; Colella, C. Disposal of Lead-Containing Zeolite Sludges in Cement Matrix. *Environ. Technol. (United Kingdom)* **1995**, *16* (2), 147–156. https://doi.org/10.1080/09593331608616255.

(44) Colella, C.; Pansini, M. Lead Removal from Wastewaters Using Chabazite Tuff. In *ACS Symposium Series*; Publ by ACS, 1988; pp 500–510. https://doi.org/10.1021/bk-1988-0368.ch032.

(45) Cioffi, R.; Pansini, M.; Caputo, D.; Colella, C. Evaluation of Mechanical and Leaching Properties of Cement-Based Solidified Materials Encapsulating Cd-Exchanged Natural Zeolites. *Environ. Technol. (United Kingdom)* **1996**, *17* (11), 1215–1224. https://doi.org/10.1080/09593331708616491.

(46) Pansini, M.; De Gennaro, R.; Parlato, L.; De'Gennaro, M.; Langella, A.; Marocco, A.; Cappelletti, P.; Mercurio, M. Use of Sawing Waste from Zeolitic Tuffs in the Manufacture of Ceramics. *Adv. Mater. Sci. Eng.* **2010**, *2010*. https://doi.org/10.1155/2010/820541.

(47) de' Gennaro, R.; Cappelletti, P.; Cerri, G.; de' Gennaro, M.; Dondi, M.; Guarini, G.; Langella, A.; Naimo, D. Influence of Zeolites on the Sintering and Technological Properties of Porcelain Stoneware Tiles. *J. Eur. Ceram. Soc.* **2003**, *23* (13), 2237–2245. https://doi.org/10.1016/S0955-2219(03)00086-4.

(48) de Gennaro, R.; Dondi, M.; Cappelletti, P.; Cerri, G.; de' Gennaro, M.; Guarini, G.; Langella, A.; Parlato, L.; Zanelli, C. Zeolite-Feldspar Epiclastic Rocks as Flux in Ceramic Tile Manufacturing. *Microporous Mesoporous Mater.* **2007**, *105* (3), 273–278. https://doi.org/10.1016/j.micromeso.2007.04.023.

(49) de Gennaro, R.; Langella, A.; D'Amore, M.; Dondi, M.; Colella, A.; Cappelletti, P.; de' Gennaro, M. Use of Zeolite-Rich Rocks and Waste Materials for the Production of Structural Lightweight Concretes. *Appl. Clay Sci.* **2008**, *41* (1–2), 61–72. https://doi.org/10.1016/j.clay.2007.09.008.

(50) de Gennaro, R.; Cappelletti, P.; Cerri, G.; de' Gennaro, M.; Dondi, M.; Graziano, S. F.; Langella, A. Campanian Ignimbrite as Raw Material for Lightweight Aggregates. *Appl. Clay Sci.* **2007**, *37* (1–2), 115–126. https://doi.org/10.1016/j.clay.2006.11.004.

(51) de' Gennaro, R.; Cappelletti, P.; Cerri, G.; de' Gennaro, M.; Dondi, M.; Langella, A. Zeolitic Tuffs as Raw Materials for Lightweight Aggregates. *Appl. Clay Sci.* **2004**, *25* (1–2), 71–81. https://doi.org/10.1016/j.clay.2003.08.005.

(52) Mercurio, M.; Bish, D. L.; Cappelletti, P.; de Gennaro, B.; de Gennaro, M.; Grifa, C.; Izzo,

F.; Mercurio, V.; Morra, V.; Langella, A. The Combined Use of Steam-Treated Bentonites and Natural Zeolites in the Oenological Refining Process. *Mineral. Mag.* **2016**, *80* (2), 347–362. https://doi.org/10.1180/minmag.2016.080.004.

(53) Cappelletti, P.; Rapisardo, G.; De Gennaro, B.; Colella, A.; Langella, A.; Graziano, S. F.; Bish, D. L.; De Gennaro, M. Immobilization of Cs and Sr in Aluminosilicate Matrices Derived from Natural Zeolites. *J. Nucl. Mater.* **2011**, *414* (3), 451–457. https://doi.org/10.1016/j.jnucmat.2011.05.032.

(54) Mercurio, M. .; Langella, A. .; Cappelletti, P. .; de Gennaro, B. .; Monetti, V. .; de Gennaro M. May the Use of Italian Volcanic Zeolite-Rich Tuffs as Additives in Animal Diet Represent a Risk for the Human Health? . *Period. di Mineral.* **2012**, *81* (3), 393–407.

(55) Cappelletti, P.; Colella, A.; Langella, A.; Mercurio, M.; Catalanotti, L.; Monetti, V.; de Gennaro, B. Use of Surface Modified Natural Zeolite (SMNZ) in Pharmaceutical Preparations Part 1. Mineralogical and Technological Characterization of Some Industrial Zeolite-Rich Rocks. *Microporous Mesoporous Mater.* **2017**, *250*, 232–244. https://doi.org/10.1016/j.micromeso.2015.05.048.

(56) Basile, A.; Cacciola, G.; Colella, C.; Mercadante, L.; Pansini, M. Thermal Conductivity of Natural Zeolite-PTFE Composites. *Heat Recover. Syst. CHP* **1992**, *12* (6), 497–503. https://doi.org/10.1016/0890-4332(92)90018-D.

(57) Baerlocher, C. .; Meier, W. M. .; Olson, D. H. *Atlas of Zeolite Framework Types* ; Elsevier, 2001.

(58) Dell'Agli, G.; Ferone, C.; Mascolo, G.; Pansini, M. Crystallization of Monoclinic Zirconia from Metastable Phases. *Solid State Ionics* **2000**, *127* (3), 223–230. https://doi.org/10.1016/S0167-2738(99)00279-9.

(59) Clayden, N. J.; Esposito, S.; Ferone, C.; Pansini, M. 29SI and 27Al NMR Study of the Thermal Transformation of Barium Exchanged Zeolite-A to Celsian. *J. Mater. Chem.* **2003**, *13* (7), 1681–1685. https://doi.org/10.1039/b212717b.

(60) Marocco, A.; Liguori, B.; Dell'Agli, G.; Pansini, M. Sintering Behaviour of Celsian Based Ceramics Obtained from the Thermal Conversion of (Ba, Sr)-Exchanged Zeolite A. *J. Eur. Ceram. Soc.* **2011**, *31* (11), 1965–1973. https://doi.org/10.1016/j.jeurceramsoc.2011.04.028.

(61) Ferone, C.; Liguori, B.; Marocco, A.; Anaclerio, S.; Pansini, M.; Colella, C. Monoclinic (Ba, Sr)-Celsian by Thermal Treatment of (Ba, Sr)-Exchanged Zeolite A. *Microporous Mesoporous Mater.* **2010**, *134* (1–3), 65–71. https://doi.org/10.1016/j.micromeso.2010.05.008.

(62) Weidenthaler, C.; Zibrowius, B.; Schimanke, J.; Mao, Y.; Mienert, B.; Bill, E.; Schmidt, W. Oxidation Behavior of Ferrous Cations during Ion Exchange into Zeolites under Atmospheric Conditions. *Microporous Mesoporous Mater.* **2005**, *84* (1–3), 302–317. https://doi.org/10.1016/j.micromeso.2005.04.022.

(63) Colantuono, A.; Dal Vecchio, S.; Mascolo, G.; Pansini, M. Thermal Shrinkage of Various Cation Forms of Zeolite A. *Thermochim. Acta* **1997**, *296* (1–2), 59–66. https://doi.org/10.1016/s0040-6031(97)00065-8.

(64) Marocco, A.; Dell'Agli, G.; Spiridigliozzi, L.; Esposito, S.; Pansini, M. The Multifarious Aspects of the Thermal Conversion of Ba-Exchanged Zeolite A to Monoclinic Celsian. *Microporous and Mesoporous Materials*. Elsevier B.V. January 15, 2018, pp 235–250.

https://doi.org/10.1016/j.micromeso.2017.08.018.

(65) Gualtieri, A. F. Accuracy of XRPD QPA Using the Combined Rietveld-RIR Method. *J. Appl. Crystallogr.* **2000**, *33* (2), 267–278. https://doi.org/10.1107/S002188989901643X.

(66) Larson, A. C. and Von Dreele, R. B. GSAS General Structure Analysis System, LANSCE ,MS-H80. *Los Alamos Natl. Lab.* **1998**, No. Los Alamos,NM 87545, USA,.

(67) Toby, B. H. EXPGUI, a Graphical User Interface for GSAS. *J. Appl. Crystallogr.* **2001**, *34* (2), 210–213. https://doi.org/10.1107/S0021889801002242.

(68) Strangway, D. W.; Chapman, W. B.; Olhoeft, G. R.; Carnes, J. Electrical Properties of Lunar Soil Dependence on Frequency, Temperature and Moisture. *Earth Planet. Sci. Lett.* **1972**, *16* (2), 275–281. https://doi.org/10.1016/0012-821X(72)90203-8.

(69) Alvarez, R. Lunar Powder Simulator under Lunarlike Conditions: Dielectric Properties. *J. Geophys. Res.* **1973**, *78* (29), 6833–6844. https://doi.org/10.1029/JB078i029p06833.

(70) Cruciani, G. Zeolites upon Heating: Factors Governing Their Thermal Stability and Structural Changes. *J. Phys. Chem. Solids* **2006**, *67* (9–10), 1973–1994. https://doi.org/10.1016/j.jpcs.2006.05.057.

(71) Charkhi, A.; Kazemian, H.; Kazemeini, M. Optimized Experimental Design for Natural Clinoptilolite Zeolite Ball Milling to Produce Nano Powders. *Powder Technol.* **2010**, *203* (2), 389–396. https://doi.org/10.1016/j.powtec.2010.05.034.

(72) Budnyak, T. M.; Yanovska, E. S.; Kichkiruk, O. Y.; Sternik, D.; Tertykh, V. A. Natural Minerals Coated by Biopolymer Chitosan: Synthesis, Physicochemical, and Adsorption Properties. *Nanoscale Res. Lett.* **2016**, *11* (1), 492. https://doi.org/10.1186/s11671-016-1696-y.

(73) García, J. E.; González, M. M.; Notario, J. S. Phenol Adsorption on Natural Phillipsite. *React. Polym.* **1993**, *21* (3), 171–176. https://doi.org/10.1016/0923-1137(93)90119-Z.

(74) Sing, K. S. W.; Williams, R. T. Physisorption Hysteresis Loops and the Characterization of Nanoporous Materials. *Adsorpt. Sci. Technol.* **2004**, *22* (10), 773–782. https://doi.org/10.1260/0263617053499032.

(75) Potter, D. K.; Corbett, P. W. M.; Barclay, S. A.; Haszeldine, R. S. Quantification of Illite Content in Sedimentary Rocks Using Magnetic Susceptibility - A Rapid Complement or Alternative to X-Ray Diffraction. *J. Sediment. Res.* **2004**, *74* (5), 730–735. https://doi.org/10.1306/021304740730.

(76) Kandapallil, B.; Colborn, R. E.; Bonitatibus, P. J.; Johnson, F. Synthesis of High Magnetization Fe and FeCo Nanoparticles by High Temperature Chemical Reduction. *J. Magn. Magn. Mater.* **2015**, *378*, 535–538. https://doi.org/10.1016/j.jmmm.2014.11.074.

(77) Kin, M.; Kura, H.; Tanaka, M.; Hayashi, Y.; Hasaegawa, J.; Ogawa, T. Improvement of Saturation Magnetization of Fe Nanoparticles by Post-Annealing in a Hydrogen Gas Atmosphere. *J. Appl. Phys.* **2015**, *117* (17), 17E714. https://doi.org/10.1063/1.4919050.

(78) Margeat, O.; Respaud, M.; Amiens, C.; Lecante, P.; Chaudret, B. Ultrafine Metallic Fe Nanoparticles: Synthesis, Structure and Magnetism. *Beilstein J. Nanotechnol.* **2010**, *1* (1), 108–118. https://doi.org/10.3762/bjnano.1.13.

(79) Barrera, G.; Sciancalepore, C.; Messori, M.; Allia, P.; Tiberto, P.; Bondioli, F. Magnetite-Epoxy Nanocomposites Obtained by the Reactive Suspension Method: Microstructural, Thermo-Mechanical and Magnetic Properties. *Eur. Polym. J.* **2017**, *94*, 354–365. https://doi.org/10.1016/j.eurpolymj.2017.07.022.

(80) Allia, P.; Barrera, G.; Tiberto, P. Linearized Rate-Equation Approach for Double-Well Systems: Cooling- and Temperature-Dependent Low-Field Magnetization of Magnetic Nanoparticles. *Phys. Rev. B* **2018**, *98* (13), 134423. https://doi.org/10.1103/PhysRevB.98.134423.

(81) Mamiya, H.; Ohnuma, M.; Nakatani, I.; Furubayashim, T. Extraction of Blocking Temperature Distribution from Zero-Field-Cooled and Field-Cooled Magnetization Curves. In *IEEE Transactions on Magnetics*; 2005; Vol. 41, pp 3394–3396. https://doi.org/10.1109/TMAG.2005.855205.

(82) Sciancalepore, C.; Bondioli, F.; Messori, M.; Barrera, G.; Tiberto, P.; Allia, P. Epoxy Nanocomposites Functionalized with in Situ Generated Magnetite Nanocrystals: Microstructure, Magnetic Properties, Interaction among Magnetic Particles. *Polymer (Guildf).* **2015**, *59*, 278–289. https://doi.org/10.1016/j.polymer.2014.12.047.

(83) Ibusuki, T.; Kojima, S.; Kitakami, O.; Shimada, Y. Magnetic Anisotropy and Behaviors of Fe Nanoparticles. *IEEE Trans. Magn.* **2001**, *37* (4), 2223–2225. https://doi.org/10.1109/20.951130.

(84) Shah, L. R.; Ali, B.; Hasanain, S. K.; Mumtaz, A.; Baker, C.; Shah, S. I. Effective Magnetic Anisotropy and Coercivity in Fe Nanoparticles Prepared by Inert Gas Condensation. *Int. J. Mod. Phys. B* **2006**, *20* (1), 37–47. https://doi.org/10.1142/S0217979206033097.

(85) Mehdaoui, B.; Meffre, A.; Lacroix, L. M.; Carrey, J.; Lachaize, S.; Respaud, M.; Gougeon, M.; Chaudret, B. Magnetic Anisotropy Determination and Magnetic Hyperthermia Properties of Small Fe Nanoparticles in the Superparamagnetic Regime. *J. Appl. Phys.* **2010**, *107* (9), 25. https://doi.org/10.1063/1.3348795.

(86) Peddis, D.; Qureshi, M. T.; Baker, S. H.; Binns, C.; Roy, M.; Laureti, S.; Fiorani, D.; Nordblad, P.; Mathieu, R. Magnetic Anisotropy and Magnetization Dynamics of Fe Nanoparticles Embedded in Cr and Ag Matrices. *Philos. Mag.* **2015**, *95* (33), 3798–3807. https://doi.org/10.1080/14786435.2015.1090640.

(87) Kalogeras, I. M.; Vassilikou-Dova, A. Electrical Properties of Zeolitic Catalysts. *Defect Diffus. Forum* **1998**, *164* (164), 1–36. https://doi.org/10.4028/www.scientific.net/ddf.164.1.

Only for Table Of Content